Extracellular Vesicle–Mediated O-GlcNAcase Transfer Drives Neuronal Necroptosis to Facilitate Gallbladder Cancer Perineural Invasion

Jingwei Zhao[1,2,3,4], Jiayun Zhu[1,2,3,4], Ziyi Yang[1,2,3,4], Yangyang Zhai[1,2,3,4], Cheng Zhao[1,2,3,4], Zhichao Lu[5], Danyang Shen[6], Qiuyi Tang[1,2,3,4], Xiaoling Song[1,2,3,4], Lin Jiang[1,2,3,4], Wenting Dai[1,2,3,4], Yaxuan Wang[7], Yidi Zhu[1,2,3,4], Liuqing Shi[1,2,3,4], Runfa Bao[1,2,3,4], Zhimin Geng[8], Ziheng Wang[9], Shilei Liu[1,2,3,4], and Wei Gong[1,2,3,4]

ABSTRACT

Peripheral nerve invasion (PNI) is an early and decisive step in gallbladder cancer progression that strongly predicts poor postsurgical outcome. The tumor–neuron interactions that drive PNI could represent potential targets and biomarkers to improve treatment of gallbladder cancer. In this study, we demonstrated that gallbladder cancer provoked necroptosis of neurons to enable PNI. Gallbladder cancer cells transferred extracellular vesicles (EV) containing O-GlcNAcase (OGA) to neurons, which activated RIPK1-dependent necroptosis. Mechanistically, EV-derived OGA suppressed RIPK1 glycosylation while enhancing its phosphorylation, thereby activating the RIPK1/RIPK3/MLKL axis to trigger neuronal necroptosis. Subsequent neuronal release of HMGB1 engaged RAGE on gallbladder cancer cells, establishing a loop that accelerated PNI. Moreover, the RAGE antagonist FPS-ZM1 synergized with gemcitabine to suppress tumor progression. Collectively, these findings uncover an EV-mediated cross-talk between gallbladder cancer cells and neurons in which RIPK1-dependent necroptosis and its effector HMGB1 drive PNI, positioning the HMGB1–RAGE axis as a tractable therapeutic target.

Significance: Tumor-derived extracellular vesicles trigger neuronal necroptosis that fuels peripheral nerve invasion, creating a tumor-neuron signaling loop that could be leveraged for liquid biopsy and personalized therapy strategies in neurotropic cancers.

Introduction

Gallbladder cancer is a highly aggressive malignancy of the digestive system, characterized by its propensity early metastasis and high recurrence rates, which contributes to its poor prognosis with a 5-year survival rate ranging from 5% to 10% (1–5). Perineural invasion (PNI), a critical factor affecting surgical outcomes, is observed in up to 71% of gallbladder cancer cases, with its incidence escalating to 96% when the tumor extends into the extrahepatic bile duct (6–8). PNI is a significant adverse prognostic factor in advanced stages of gallbladder cancer, yet the precise mechanisms underlying the PNI by gallbladder cancer remain elusive (9–11).

The concept that PNI involves "active invasion by cancer cells rather than passive diffusion" has garnered considerable attention (12–14). Tumor–neuron interactions, particularly those mediated by extracellular vesicles (EV), are highlighted as one of the central aspects to understand tumor development and potential therapeutic intervention (15–17). PNI is regulated by dynamic signaling between tumor cells and nerve fibers, encompassing molecular, cellular, and metabolic mechanisms (18–21). However, the cellular and molecular dynamics involved in tumor–neuron interactions, especially those mediated by EVs, are still not well understood.

In the present study, molecular maps of the neural microenvironment in patients with PNI-positive and PNI-negative gallbladder cancer were constructed using laser microdissection and high-sensitivity mass spectrometry. By analyzing protein changes in neurons within PNI regions, key alterations in nerves were identified after invasion. Notably, we found a significant increase in O-GlcNAcase (OGA) expression within invaded nerves. Clinical cohort analysis confirmed that elevated OGA expression in neurons is associated with both PNI intensity and overall survival (OS). To further investigate the role of EVs in tumor–neuron interactions, we established a noncontact coculture system of gallbladder cancer cells and neurons using standardized EV extraction and characterization techniques, as well as untargeted metabolomics. Our findings suggested that gallbladder cancer cells transfer OGA to neurons via the EV pathway. Subsequent

[1]Department of General Surgery, Xinhua Hospital, Affiliated to Shanghai Jiao Tong University School of Medicine, Shanghai, China. [2]Shanghai Key Laboratory of Biliary Tract Disease Research, Shanghai, China. [3]Shanghai Research Center of Biliary Tract Disease, Shanghai, China. [4]Biliary Disease Research Institute of Shanghai Jiao Tong University School of Medicine, Shanghai, China. [5]Department of Neurosurgery, Research Center of Clinical Medicine, Affiliated Hospital of Nantong University, Nantong, China. [6]Department of General Surgery, The First Affiliated Hospital of Soochow University, Suzhou, China. [7]Department of Urology, The First Affiliated Hospital of Harbin Medical University, Harbin, China. [8]Department of Hepatobiliary Surgery, the First Affiliated Hospital of Xi'an Jiao Tong University, Xi'an, China. [9]MOE Frontier Science Centre for Precision Oncology, University of Macau, Macau SAR, China.

J. Zhao, J. Zhu, and Z. Yang contributed equally to this article.

Corresponding Authors: Wei Gong, Department of General Surgery, Xinhua Hospital, Affiliated to Shanghai Jiao Tong University School of Medicine, Shanghai 200092, China. E-mail: gongwei@xinhuamed.com.cn; Shilei Liu: lsl81106626@alumni.sjtu.edu.cn; Ziheng Wang, MOE Frontier Science Centre for Precision Oncology, University of Macau, Macau SAR 999078, China. E-mail: zihengwang@um.edu.mo; and Zhimin Geng, Department of Hepatobiliary Surgery, the First Affiliated Hospital of Xi'an Jiao Tong University, Xi'an 710061, Shaanxi, China. E-mail: gengzhimin@mail.xjtu.edu.cn

Cancer Res 2026;86:1392–413

doi: 10.1158/0008-5472.CAN-25-2237

This open access article is distributed under the Creative Commons Attribution-NonCommercial-NoDerivatives 4.0 International (CC BY-NC-ND 4.0) license.

©2025 The Authors; Published by the American Association for Cancer Research

experiments, including metabolic drug screening, real-time cell death kinetic assays, and lactate dehydrogenase (LDH) release assays, demonstrated that EV-derived OGA induces RIPK1-dependent necroptosis in neurons. Coimmunoprecipitation (co-IP), point mutation, and glycosylation substrate complementation experiments revealed that OGA promotes RIPK1 phosphorylation while inhibiting its glycosylation, thereby activating the RIPK1/RIPK3/MLKL (complex IIb) pathway. The function of RIPK1-dependent necroptosis in the remodeling of the neural microenvironment was confirmed using dorsal root ganglion (DRG) three-dimensional (3D) coculture models, nude mouse sciatic nerve invasion models, and adeno-associated virus (AAV)-mediated neuronal RIPK1 knockdown models. Finally, we revealed the molecular pathway by which HMGB1, released from necroptotic neurons, enhances gallbladder cancer invasion via the RAGE receptor. In summary, our study demonstrates that gallbladder cancer cells transfer OGA to neurons through the exosomal pathway. By inhibiting RIPK1 glycosylation and promoting its phosphorylation, OGA induces necroptosis in neurons, causing neuronal rupture and subsequent HMGB1 release. HMGB1 activates RAGE receptors on gallbladder cancer cells, thereby promoting neurotropic invasion. Additionally, FPS-ZM1, a high-affinity RAGE receptor inhibitor, exhibited synergistic effect with gemcitabine, enhancing anticancer efficacy against gallbladder cancer.

Materials and Methods

Patient enrollment and sample collection

This study retrospectively analyzed 66 patients with gallbladder cancer undergoing surgical resection at Xinhua Hospital, Shanghai Jiao Tong University School of Medicine, from January 2013 to December 2021. Studies were conducted in accordance with International Ethical Guidelines for Biomedical Research Involving Human Subjects (Council for International Organizations of Medical Sciences). Patients who received preoperative chemotherapy or radiotherapy were excluded from the study. Written informed consent was obtained from all participants, and the study was conducted with the approval of the Ethics Committee of Xinhua Hospital (No. XHEC-C-2021-095-2). All collected tumor specimens underwent fixation in 10% neutral buffered formalin and were then embedded in paraffin using established laboratory methods. Paraffin-embedded tissue sections were prepared and subjected to hematoxylin and eosin (H&E) staining by Servicebio Inc. The H&E staining procedure was performed as follows: sections were stained with hematoxylin for 5 to 8 minutes, rinsed in tap water, differentiated in 1% hydrochloric acid ethanol, and returned to blue. Subsequently, eosin was then applied as a counterstain for 1 to 2 minutes, with the procedure concluding through dehydration in graded ethanol, xylene clearing, and mounting in neutral resin. Microscopic examination was performed using a Leica DMi8 upright optical microscope. Images were captured under 10×, 20×, and 40× objectives using a camera integrated with the microscope system. All images were saved in Tagged Image File Format for subsequent analysis. The criterion for PNI was tumor cell involvement of ≥33% of the nerve perimeter or confirmed invasion into the nerve sheath layers (epineurium, perineurium, and endoneurium). PNI severity was assessed based on two parameters: the extent and frequency of neural invasion. The invasion extent was scored as follows: 0 (none), 1 (perineural type, tumor encircling ≥33% of the nerve), and 2 (intraneural type, tumor infiltrating the nerve sheath). Frequency was scored as follows: 0 (none), 1 (occasional), 2 (frequent), and 3 (highly frequent). A composite PNI score was derived from the product of invasion extent and frequency. Disease severity was then graded as mild (score of 2), moderate (score of 3), or severe (score of 4 or higher) based on this calculation. For subsequent analysis, PNI-positive cases were defined as those with a score of 2 to 5, and PNI-negative cases as those with a score of 0 to 1. Two independent, experienced pathologists, blinded to clinical data, performed all histologic evaluations. Any discrepant assessments were adjudicated by a third senior pathologist to establish a final consensus.

Clinical feature analysis

Based on postoperative H&E staining, PNI status was assessed, and patients were categorized into PNI-positive ($n = 39$) and PNI-negative ($n = 27$) groups. Subsequent to this analysis, which compared survival distributions via the Mantel–Cox test between PNI-positive and PNI-negative groups, immunohistochemistry (IHC) staining was performed to further evaluate the prognostic significance of OGA expression in the former. Patients were stratified into low-, medium-, and high-expression subgroups (OGA-low, OGA-medium, and OGA-high groups) based on quantitative scoring metrics such as integrated optical density. OS was assessed as the duration from surgery until death or the last documented follow-up (in months). Kaplan–Meier curves were first plotted to compare OS between patients with and without PNI. Subsequently, a separate analysis was conducted within the PNI-positive cohort to compare OS between the OGA-medium and OGA-high expression groups. In addition to evaluating the proportional hazards assumption via Schoenfeld residual plots, the log-rank test was used to determine the statistical significance of survival differences. HRs and 95% confidence intervals (CI) were computed to estimate relative risk. A multivariate Cox proportional hazards regression model was constructed to determine whether PNI held autonomous prognostic value, when considered alongside other clinical variables, including sex, age, tumor size, histologic grade, tumor–node–metastasis stage, and OGA expression level. HRs, 95% CIs, and P values were reported for each variable. Significant associations were annotated by corresponding P values, and GraphPad Prism (RRID: SCR_002798) was used for analysis and visualization.

Single-cell transcriptomic analysis

From Xinhua Hospital Affiliated to Shanghai Jiao Tong University School of Medicine, six patients diagnosed with advanced gallbladder cancer were included in the study between July 2023 and January 2024. All six patients underwent neoadjuvant therapy (NAT), leading to significant tumor regression, followed by radical resection. Tissue samples were collected during the surgical resection, encompassing tumors ($n = 6$). Pathologic examinations were conducted to ascertain the tissue origin. To augment our analysis, we incorporated an additional 11 patients with gallbladder cancer from a previous study, for whom paired tumor and adjacent normal tissues had undergone single-cell RNA sequencing [scRNA-seq, National Omics Data Encyclopedia (NODE) ID: OEP001237]. These patients did not undergo NAT and were assigned into the control group in this study. Marker genes for each cell cluster were identified via the R package COSG (https://github.com/genecell/COSGR/), which applies a cosine similarity–driven algorithm to enable a more precise and scalable comparison of transcriptional profiles between clusters. A default two-sided Wilcoxon rank-sum test was used for the differential expression analysis, performing a comprehensive comparison of all gene expression profiles across the two datasets. Genes were defined as significantly differentially

expressed if they met the following criteria: a Bonferroni-adjusted *P* value of less than 0.05 and an absolute log-scaled fold change (FC) greater than 0.5. Cells from each cluster were annotated into various cell types according to the reference datasets of SingleR, ScType, and Celltypist. Further refinement of the cell cluster annotations was informed by the panel of cluster-specific, upregulated marker genes identified through differential expression analysis.

H&E, immunofluorescence, and IHC staining

The tissue samples used in this study included human gallbladder cancer tissues and sciatic nerves from nude mice invaded by tumor cells. All specimens were processed and paraffin-embedded according to the following protocol. Upon harvest, tissues were immediately placed in neutral formalin for fixation at room temperature for a minimum of 24 hours and were subsequently maintained in the same fixative for storage and transport. After fixation, target tissue areas were trimmed with a scalpel in a fume hood to ensure flat surfaces and then placed in dehydration cassettes with corresponding labels for embedding preparation. The dehydration protocol consisted of a graded ethanol series (75% for 4 hours, 85% for 2 hours, and 90% for 2 hours, 95% for 1 hour) followed by two 30-minute incubations in absolute ethanol. Subsequent transitions included a 5- to 10-minute alcohol–xylene step and two final 5- to 10-minute xylene washes. Samples were then transferred to 65°C paraffin wax for three rounds of infiltration, each lasting 1 hour. Following dehydration, tissues were embedded in paraffin using an automated embedding station. The process involved orienting the tissues in molds prefilled with molten paraffin, into which they were swiftly transferred from the dehydration cassettes. Following labeling before paraffin hardening, the embedded blocks were serially cooled at −20°C, demolded, and trimmed. The ribboned sections were processed by floating on a 40°C water bath, mounting onto slides, and baking at 60°C to ensure adhesion and complete wax removal. Completed sections were stored at room temperature for future experiments. H&E staining was performed through a series of steps: deparaffinization, rehydration, and H&E staining according to the specified durations, with intermediary rinsing, differentiation, and bluing, concluding with dehydration, clearing, and final mounting.

To assess the localization of tumor and neuronal markers, CK19 (Abcam, ab76539, RRID: AB_1523469) and TUJ1 (Abcam, ab18207, RRID: AB_444319) were used for dual immunofluorescence (IF) staining, with DAPI applied for nuclear counterstaining. Paraffin-embedded tissue sections from patients with gallbladder cancer or sciatic nerves from tumor-infiltrated nude mice were processed for double staining using primary antibodies derived from different host species. Tissue sections underwent deparaffinization through sequential xylene immersions (three changes, 10 minutes each) and were rehydrated in a graded ethanol series, concluding with a thorough distilled water rinse. Antigen retrieval was then conducted following the primary antibody–specific protocol, with meticulous care to prevent buffer evaporation and tissue desiccation. After cooling to room temperature, the sections were subjected to three 5-minute PBS (pH 7.4) washes on a shaker. Prior to blocking, a hydrophobic barrier was created around the tissue with a hydrophobic barrier PAP pen. The sections were then incubated in 3% BSA for 30 minutes at room temperature to prevent nonspecific binding. For goat primary antibodies, 10% donkey serum was substituted for blocking. For primary antibody incubation, a mixture of the two antibodies (raised in different species) was applied at optimal dilutions, and slides were kept at 4°C overnight in a humidified box. Subsequently, after thorough washing in PBS (3 × 5 minutes), a mixture of fluorescently labeled secondary antibodies specific to the primary antibody hosts was introduced. After three additional PBS washes after secondary antibody incubation, nuclear staining was performed using DAPI (10 minutes, dark). Autofluorescence was suppressed by a 5-minute treatment with quenching reagent B, followed by a 10-minute running water rinse. Coverslips were applied with antifade mounting medium to complete the preparation, with antibody details cataloged in Supplementary Table S1.

Paraffin-embedded gallbladder cancer tissues and sciatic nerve tissues invaded by gallbladder cancer cells in nude mice were subjected to IHC staining for OGA. Following a standard protocol of dewaxing and ethanol gradient rehydration, heat-induced antigen retrieval was carried out in suitable buffers. Subsequent to cooling and PBS washes, endogenous peroxidases were blocked by the application of 3% hydrogen peroxide for 25 minutes under dark conditions. Nonspecific binding was blocked with 3% BSA for 30 minutes at room temperature. Primary immunolabeling was performed using anti-OGA antibody (1:200, Abcam, ab197389, RRID: AB_3711368) during an overnight incubation at 4°C. Secondary detection was carried out after PBS washes by applying the matching horseradish peroxidase (HRP)-conjugated secondary antibody for 50 minutes at room temperature. Signals were developed with 3,3′-diaminobenzidine substrate, monitored under a microscope, and terminated with tap water. After hematoxylin counterstaining with subsequent differentiation and bluing, the sections underwent sequential processing through graded ethanol dehydration, n-butanol and xylene clearing, and mounting in neutral resin. IHC images were acquired under a bright-field microscope with consistent imaging settings across samples. OGA expression levels were quantified using ImageJ (RRID: SCR_003070) by assessing staining intensity and positive staining area. Quartile-based classification was utilized to categorize the samples into three tiers: low, intermediate, and high expression. A dual assessment of all scores was conducted independently by two blinded investigators, with the mean value calculated for subsequent analysis. All statistical analyses and data visualization were performed using GraphPad Prism software (RRID: SCR_002798).

Laser-assisted proteomics

A proteomic analysis was conducted on gallbladder cancer tissues resected at Xinhua Hospital during the 2023 to 2025 timeframe to characterize the protein expression signatures correlated with PNI. All enrolled cases were histopathologically confirmed as gallbladder cancer. Furthermore, no patient had a history of neoadjuvant chemotherapy or radiotherapy before the surgical procedure. In each sample, both PNI-positive and PNI-negative regions were identified for analysis. All tissues were snap-frozen and sectioned into consecutive 10-μm-thick cryosections. H&E staining, IF, and IHC were performed on adjacent sections to facilitate spatial localization and morphologic confirmation. PNI-positive and PNI-negative regions were manually annotated based on the stained images. Laser microdissection was used to precisely isolate the targeted regions of interest. The microdissected tissues were lysed, and proteins were extracted and digested with trypsin. Prior to LC/MS-MS analysis, the resulting peptides were concentrated via nanofiltration. Protein identification and quantification were achieved by processing the raw spectral data through MaxQuant (RRID: SCR_014485) and searching against the UniProt human protein database. Statistical comparisons of normalized protein expression data between PNI-positive and PNI-negative groups were performed in GraphPad Prism using unpaired two-tailed *t* tests (for two groups) or one-way

ANOVA with the Tukey *post hoc* test (for multiple groups). Values are shown as the mean ± SD, and a P value of less than 0.05 was considered statistically significant. For each protein, FC values were calculated, and statistical significance was determined. A volcano plot was constructed in GraphPad Prism to visualize differentially expressed proteins, with the vertical axis (y-axis) indicating the $\log_2$ FC and the horizontal axis (x-axis) showing the protein ranking. Applying the significance thresholds of $P < 0.05$ and an absolute FC greater than 2, we identified differentially expressed proteins, among which, OGA was selected for subsequent analysis.

Noncontact coculture system of neuron and gallbladder cancer cells

All cell-based assays were conducted using an EV-free FBS culture system, specifically designed to avoid confounding effects from serum-derived vesicles. The EV-free FBS used (MeilunBio, PWL218) was prepared by ultracentrifugation (>100,000 × *g*, 4°C, 10 hours) and 0.22 μm filtration to remove EV contamination. Before any treatment or experimental manipulation, all cell lines were cultured in EV-free medium for at least 24 hours to eliminate any residual vesicles that may have been adsorbed or internalized under conventional culture conditions, thereby ensuring the reliability and reproducibility of EV extraction and subsequent functional assays. Human neurons were obtained by a two-step division method using the SH-SY5Y differentiation method of Shipley and colleagues (22). This study utilized two human gallbladder cancer cell lines: NOZ from the Health Sciences Research Resources Bank, Japan, and GBC-SD from the Shanghai Institute for Biological Sciences, China. All cells were cultured under standard conditions (37°C, 5% CO_2) in medium containing 10% EV-free FBS and 1% penicillin–streptomycin. Neurons were cultured according to the conditioned medium (CM) used in the culture phase. To decipher how gallbladder cancer–derived EVs in neuron–tumor interactions, a series of *in vitro* coculture models were established. In the basic coculture model, gallbladder cancer cells and primary neurons were seeded at a 1:1 ratio in a Transwell apparatus configured with 0.4-μm pores, placing tumor cells on the insert membrane and neurons in the lower chamber, respectively. This setup ensured that there was no direct cell–cell contact, allowing only indirect interaction via soluble factors or vesicles. After 48 hours of coculture, downstream functional analyses were conducted.

An EV-supplemented coculture model was implemented by introducing exogenous gallbladder cancer cell–derived EVs into the neuronal chamber of the established coculture system. Without explicit labeling, the EVs added into the cells were 1×10^6 particles/mL, and the treatment time was 48 hours. In the EV direct treatment model, neurons were cultured alone and treated directly with gallbladder cancer–derived EVs for 48 hours to evaluate the direct impact of tumor-derived EVs on neuronal function. To establish the gallbladder cancer–CM treatment model, culture supernatant was harvested from gallbladder cancer cells following a 48-hour incubation. The supernatant was then subjected to sequential centrifugation at 300 × *g* (10 minutes) and 2,000 × *g* (20 minutes) to eliminate cellular debris. Subsequently, the resulting CM, enriched in tumor-secreted factors, was then applied to neurons to assess the effect of tumor secretome on neuronal status. In the neuron-CM (CM-N) feedback model, neurons were first treated with gallbladder cancer–derived EVs for 48 hours. Following collection, the CM-N was repurposed to culture gallbladder cancer cells, thereby assessing the feedback regulatory influence of EV-modulated neuronal secretions on tumor behavior. All incubations were performed under standard conditions (37°C, 5% CO_2). The endogenous protein synthesis in neurons was inhibited by pretreatment with cycloheximide at 20 μg/mL for 2 hours. To ensure comparability, consistent EV dosages and incubation times were applied consistently to every group.

EV isolation and characterization

EVs were isolated from cell culture supernatants using a sequential centrifugation protocol designed to eliminate cells, debris, and large particles (23). To isolate EVs, cell culture medium from exogenous vesicle-free systems was processed through a sequential centrifugation protocol. An initial step at 3,000 × *g* for 10 minutes (repeated once) removed cells and debris. The supernatant was then centrifuged at 10,000 × *g* for 30 minutes to pellet large vesicles and apoptotic bodies. The resulting supernatant was used for EV enrichment via two cycles of high-speed centrifugation (12,000 × *g*, 60 minutes each) in PBS. All steps were conducted at 4°C.

To visualize the ultrastructure of gallbladder cancer–derived EVs, transmission electron microscopy (TEM) was performed. The EV suspension (10 μL) was deposited onto carbon-coated copper grids and left undisturbed for 1 minute to facilitate particle adhesion. The grids were then gently blotted with filter paper to remove unbound solution. Next, 10 μL of 2% uranyl acetate was added to the grids for negative staining for 1 minute, followed by gentle drying with filter paper. To visualize typical EV morphology, the air-dried grids were subjected to TEM analysis at an acceleration voltage of 100 kV, which enabled the identification of the characteristic round or cup-shaped structures.

EV size distribution and concentration were quantified using nanoparticle tracking analysis (NTA). A 10 μL sample was appropriately diluted in sterile PBS (Sangon Biotech, E607008), ensuring that the final concentration fell within the instrument's linear detection range and prevented needle clogging. The instrument was calibrated with standard particles prior to use to ensure performance consistency. After sample measurement, the system automatically generated output including average particle diameter, particle concentration (particles/mL), and size distribution histograms. All NTA procedures were conducted by EObiotech.

To validate the identity of isolated EVs, Western blot (WB) analysis was performed to detect classic EV marker proteins. The protein concentration of EV lysates (with protease inhibitors added to RIPA buffer) was determined by bicinchoninic acid (BCA). After SDS-PAGE separation and polyvinylidene difluoride (PVDF) membrane transfer, blocking was done with 5% nonfat milk. The membranes were then incubated overnight at 4°C with primary antibodies against EV markers, including CD63 (Abcam, ab134045, RRID: AB_2800495), TSG101 (Abcam, ab133586, RRID: AB_2943043), OGA (Abcam, ab197389, RRID: AB_3711368), GM130 (Abcam, ab169276, RRID: ab169276), and calnexin (Abcam, ab92573, RRID: AB_10563673). The next day, membranes were washed and incubated with HRP-conjugated secondary antibodies for 1 hour at room temperature. Protein bands were visualized using enhanced chemiluminescence reagents and imaged using a chemiluminescence detection system.

To track neuronal uptake of gallbladder cancer–derived EVs, the EVs were labeled with the green lipophilic dye DiO (Invitrogen, V22886). A 1 mmol/L DiO stock solution was diluted to 5 μmol/L and incubated with EVs in the dark at room temperature or 37°C for 10 to 20 minutes. Unincorporated dye was removed through either ultrafiltration and ultracentrifugation (100,000 × *g*, 70 minutes), followed by multiple PBS washes and final resuspension to obtain purified DiO EVs. Primary neurons were seeded in six-well plates

and cultured to 70% to 80% confluence. For uptake experiments, DiO-labeled EVs were incubated with cells for 4 hours at 37°C. Blank controls and unlabeled EV controls were included in parallel. After incubation, red fluorescence signals within neurons were observed under a fluorescence microscope to assess EV uptake efficiency.

WB analysis

Total protein was extracted from cells or EVs using RIPA lysis buffer (Solarbio, R0010) containing phenylmethylsulfonylfluoride (1:100, Sangon Biotech, A610425) and Protease Inhibitor Cocktail (Sangon Biotech, C600386), with concentrations determined by BCA assay (Beyotime, P0011). For immunoblotting, equal protein loads (20–40 μg) were resolved by SDS-PAGE, transferred to PVDF membranes (Millipore, ISEQ00010), and blocked with 5% nonfat milk. Membranes were incubated overnight with primary antibodies (listed in supplemental information) at 4°C, followed by TBST washes and 1-hour incubation with HRP-conjugated secondary antibodies (1:10,000, Beyotime A0208 and A0216) at room temperature. Blots were developed with enhanced chemiluminescence reagent and visualized using a GE600 imaging system. For EV protein detection, vesicle samples were isolated by ultracentrifugation, and equal amounts of protein were used for blotting. The expression of specific proteins in EVs was compared with their parent cells to validate enrichment or differential expression. Each WB procedure was carried out in at least three independent replicates. The corresponding antibody specifications are compiled in Supplementary Table S1.

In vitro modeling of tumor invasion toward neurons

Prior to the assay, Transwell insert membranes were coated with a uniform layer of Matrigel matrix (Corning, 354348) and incubated at 37°C for 1 hour to facilitate polymerization. Following experimental treatment, gallbladder cancer cells were harvested, resuspended in serum-free medium, and seeded into the inserts at a density of 1×10^5 cells per well.

To create a chemotactic gradient, cells were seeded in the upper chamber in serum-free medium, whereas the lower chamber contained complete medium supplemented with 10% EV-free FBS. Depending on the experimental design, various treatments were applied to either the upper or lower chamber. These included small-molecule interventions (e.g., specific inhibitors or agonists), EV treatment (e.g., EVs derived from NOZ, GBC-SD, or L-2F7 cells added to the lower chamber), or CM (CM-N or CM-T). After a cell line–optimized invasion period (≥24 hours), the membranes were processed by removing noninvading cells from the upper side with a swab. Cells on the lower surface were fixed with 4% paraformaldehyde (PFA), stained with 0.1% crystal violet, and quantified by counting five random microscopic fields per membrane. Invasion was calculated as the mean cell count per field multiplied by 100, with triplicates per group. Drug information is listed in Supplementary Table S2.

DRG and tumor coculture assay

DRGs were isolated from neonatal BALB/c nude mice after euthanasia by CO_2 inhalation. To prevent damage to nerve roots, cervical dislocation was not sed. All procedures from this point onward were conducted under sterile conditions. After thorough disinfection of the skin with 70% ethanol and air-drying, mice were placed in the prone position on a sterile dissection board. Using sterile scissors, a midline incision was created along the spine to reveal the underlying vertebral column. Additionally, the ribs on both sides were removed, and the entire spine was excised and rinsed twice in cold PBS. Under a stereomicroscope, the spine was placed on sterile Telfa pads or gauze, and surrounding muscle and connective tissue were removed. The vertebral lamina was cut along the spinal axis and spread open to expose the spinal cord and nerve roots. DRGs were identified as pale yellow, spherical structures. The distal intercostal nerves were cut, leaving 2 to 3 mm of the nerve stump to facilitate handling. The dorsal and ventral roots were then cut sequentially to isolate intact DRGs. Isolated ganglia were transferred into prechilled DMEM containing 10% EV-free FBS, 1% penicillin–streptomycin (Corning, 30-002-Cl), 1% sodium pyruvate (Gibco, 11360070), and 1% nonessential amino acids (Gibco, 11140050). For DRG embedding and culture, all procedures were conducted on ice using precooled pipette tips. To create a defined substrate, a 20 μL aliquot of growth factor–reduced Matrigel was deposited onto the center of a 35-mm glass-bottom dish, forming a gel spot of approximately 1 mm. A single DRG was carefully placed at the center of the extracellular matrix (ECM) using a stereomicroscope, ensuring close contact with the dish surface. After gelling at 37°C for 10 to 15 minutes in a sterile laminar flow hood, 2 mL of prewarmed neuronal culture medium (Neurobasal-A + B27 + L-glutamine + NGF at 50 ng/mL) was gently added. Under standard incubation conditions (37°C, 5% CO_2), medium changes followed a regimen of replacement on day 1 and every second day afterward. A dense neurite network was established after a 48-hour culture period prior to coculture initiation. Tumor cells (NOZ and GBC-SD cells) were first maintained in EV-free FBS medium for at least 24 hours to clear residual exogenous EVs. Subsequently, 20,000 pretreated tumor cells were washed with PBS and prepared in 40 μL of ECM suspension for coculture. Using microscopic guidance, aliquots (1–2 μL) of the cell–ECM suspension were deposited at several sites surrounding the DRG within a 500 μm radius, thereby establishing a spatially defined, noncontact coculture system. After gel solidification, prewarmed medium (neuronal medium or mixed neurotumor medium) was added, and the coculture was maintained for 24 to 72 hours to observe neurite guidance, chemotactic responses, and neuroplasticity. To assess migratory potential along nerve fibers, a nerve invasion index was derived from the ratio of outer to inner region tumor cell counts, indicative of distal migration tendency. Quantification involved independent evaluation by two blinded observers, with mean values calculated for subsequent analysis.

Establishment of the perineural invasion mouse model by sciatic nerve injection

To recapitulate gallbladder cancer PNI in an *in vivo* setting, we established a mouse model via perisciatic injection of tumor cells into immunodeficient mice. Female BALB/c nude mice (6 weeks old) were purchased from GemPharmatech Co., Ltd. The study was conducted in compliance with ethical guidelines for animal research under the approval of Xinhua Hospital's Laboratory Animal Ethics and Welfare Committee (XHEC-F-2025-054). Nude mice were acclimatized for 7 days before random assignment to experimental groups, with sample sizes determined based on prior research and established laboratory protocols. NOZ cells were enzymatically detached and suspended in an ice-cold 1:1 solution of serum-free PBS and Matrigel, achieving a final concentration of 1×10^5 cells per 10 μL. Surgical procedures were performed under isoflurane anesthesia, with mice positioned in lateral recumbency. The right hind limb was prepared by shaving and aseptic preparation, followed by a

1.5- to 2-cm incision along the lateral hip. Blunt dissection through muscular layers revealed the sciatic nerve. Under microscopic visualization, 25 μL of tumor cell suspension was precisely administered into the perineural space adjacent to the sciatic nerve using a Hamilton microsyringe (10 μL capacity, model 80330), with careful attention to preserving nerve integrity. Wound closure was achieved through layered suturing of muscle and skin tissues. Postoperative management consisted of antimicrobial prophylaxis with ceftezole (20 mg/kg, intramuscular) and analgesic support using buprenorphine as clinically indicated. Mice were monitored daily for general condition, motor function, and hind limb paralysis score. Neurologic deficits associated with PNI typically appeared within 14 days after injection. At the endpoint, mice were euthanized, and the injected sciatic nerve and surrounding tissues were collected for histologic and molecular analysis. Histologic analysis was performed on 4% PFA-fixed, paraffin-embedded tissue sections stained with H&E to examine neural architecture disruption and tumor infiltration.

siRNA-mediated gene silencing

To transiently knock down the expression of OGA or RIPK1 in cells, siRNA transfection was performed to induce gene-specific silencing. Cells were plated in either six-well (Corning, 3516) or 12-well (Corning, 3513) culture plates, and transfection procedures were commenced upon reaching 50% to 60% confluence. All transfection experiments were performed using antibiotic-free medium containing 10% EV-depleted FBS to eliminate potential confounding effects from external nucleic acids or vesicular contaminants. Human OGA and RIPK1 siRNAs were synthesized by OBiO Technology Corp., Ltd. Multiple siRNA sequences targeting each gene were screened to identify effective silencing candidates. For control purposes, a scrambled siRNA sequence was used as the negative control.

Gene silencing transfections were performed with Lipofectamine RNAiMAX reagent according to the manufacturer's specifications. siRNA oligonucleotides were prepared at 30 nmol/L in Opti-MEM medium and complexed with the transfection reagent through a 15-minute incubation at ambient temperature. These complexes were then applied directly to cultured cells. Following 6 hours of exposure, the transfection medium was replaced with complete medium supplemented with 10% EV-free FBS, and cells were cultured until the predetermined endpoints. Cellular samples were collected 48 to 72 hours after transfection for subsequent examination. Knockdown efficiency was verified through immunoblotting assessment of OGA and RIPK1 protein expression. All transfection assays included a minimum of three independent biological replicates to ensure experimental reproducibility and statistical robustness.

The following siRNA sequences were utilized for gene silencing. siOGA-1: GCAGUUACUUGGCUGAUCUA; siOGA-2: GGCACUUUUCUGUUUAUCCAA; siOGA-3: CAGAAACUUUCCUUUGCUAA; siRIPK1-1: GAAAGAGUAUUCAAACGAATT; siRIPK1-2: GACGAGUUCAUCACUACUATT; and siRIPK1-3: GAGUAAACUCCAAGACGAATT.

Untargeted metabolomic profiling of neurons after EV treatment

To investigate metabolic alterations induced by EVs, neurons were treated with approximately 3×10^6 particles/mL of EVs for 24 hours. For intracellular metabolite extraction, cells were washed with warm PBS after treatment, followed by the addition of 800 μL ice-cold methanol/acetonitrile (1:1) for protein precipitation. After vortexing and centrifugation (14,000 × *g*, 20 minutes), the supernatant was vacuum-dried, reconstituted in acetonitrile/water (1:1), and centrifuged again. The final extract was analyzed by LC/MS. For quality control, a pooled sample from each experimental aliquot was injected after every five runs to ensure system stability. Metabolomic analysis was carried out by Shanghai Applied Protein Technology Co., Ltd. using ultra-high performance liquid chromatography (Vanquish UHPLC system, Thermo Fisher Scientific) coupled with high-resolution mass spectrometry (Orbitrap Exploris 480). Separation was achieved on an ACQUITY UPLC BEH Amide column (2.1 × 100 mm, 1.7 μm; Waters) with a binary mobile phase consisting of (A) 25 mmol/L ammonium acetate and ammonium hydroxide in water and (B) acetonitrile. The gradient program was as follows: 95% B (0.5 minutes), 95%→65% B (6.5 minutes), 65%→40% B (1 minute), and 40% B (1 minute), followed by rapid re-equilibration. MS detection was performed in both positive and negative electrospray ionization modes under the following source conditions: sheath gas 50, auxiliary gas 2, capillary temperature 350°C, and spray voltages of +3.5 kV (positive) and −2.8 kV (negative). Full scan spectra (m/z 70–1,200) were acquired at 60,000 resolution, with data-dependent MS-MS acquisition incorporating a 4-second dynamic exclusion window. Raw data were processed and normalized to the total ion current. Multivariate statistical approaches were used to analyze the metabolomic data, incorporating both principal component analysis and orthogonal partial least squares-discriminant analysis with Pareto scaling. Model validation was conducted through 7-fold cross-validation and permutation tests. Metabolites meeting the criteria of variable importance in projection scores exceeding 1.0 and statistical significance ($P < 0.05$, determined by Student *t* test) were identified as differentially abundant.

Crystal violet staining assay

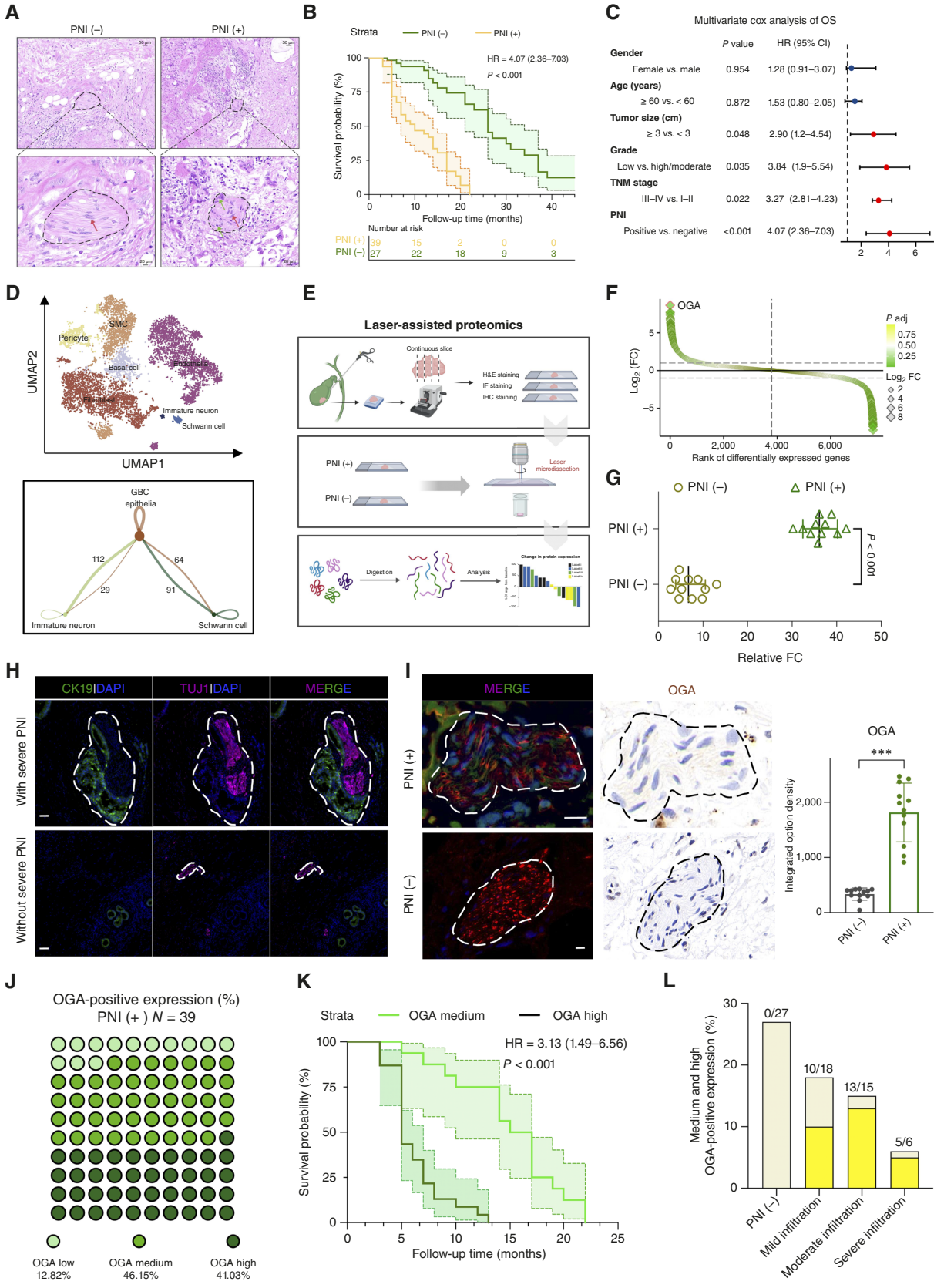
To assess neuronal cell viability after treatment with EVs derived from NOZ cells, crystal violet staining was performed. Neuronal cultures plated in 24-well plates received designated treatments according to experimental design. Following intervention, cellular monolayers were carefully rinsed twice with PBS to eliminate nonviable and detached cells. The adherent cell population was fixed using 4% PFA solution for 15 minutes and subsequently washed with PBS.

Cell Counting Kit-8 assay

Neuronal viability was determined by Cell Counting Kit-8 (CCK8) assay (MedChemExpress, HY-K0301) after NOZ-EV treatment. Following exposure, 10 μL CCK8 was added to 100 μL medium in 96-well plates. After 2-hour incubation in the dark at 37°C, absorbance was measured at 450 nm. Triplicate data were normalized to control and analyzed by one-way ANOVA (significant at $P < 0.05$).

Compound library screening for cancer metabolic modulators

To identify potential small-molecule compounds that could reverse EV-induced neuronal metabolic alterations, a functional rescue screening was performed using a cancer metabolism–focused compound library (L5700, TargetMol). Neurons were cultured under standard conditions, and once 70% to 80% confluence was reached, they were treated with NOZ-derived EVs for 24 hours to mimic the tumor-derived EV intervention. The L5700 compound library comprises 339 small molecules targeting key metabolic pathways, including glycolysis, hexosamine biosynthetic pathway,


A
PNI (–)
PNI (+)
B
Strata
PNI (–)
PNI (+)
HR = 4.07 (2.36–7.03)
P < 0.001
Survival probability (%)
Follow-up time (months)
Number at risk
PNI (+) 39 15 2 0 0
PNI (–) 27 22 18 9 3
C
Multivariate cox analysis of OS
P value
HR (95% CI)
Gender
Female vs. male 0.954 1.28 (0.91–3.07)
Age (years)
≥ 60 vs. < 60 0.872 1.53 (0.80–2.05)
Tumor size (cm)
≥ 3 vs. < 3 0.048 2.90 (1.2–4.54)
Grade
Low vs. high/moderate 0.035 3.84 (1.9–5.54)
TNM stage
III–IV vs. I–II 0.022 3.27 (2.81–4.23)
PNI
Positive vs. negative <0.001 4.07 (2.36–7.03)
D
UMAP2
UMAP1
SMC
Pericyte
Basal cell
Endothelial
Fibroblast
Immature neuron
Schwann cell
GBC epithelia
112
64
29
91
Immature neuron
Schwann cell
E
Laser-assisted proteomics
Continuous slice
H&E staining
IF staining
IHC staining
PNI (+)
PNI (–)
Laser microdissection
Digestion
Analysis
F
OGA
P adj
Log2 FC
Rank of differentially expressed genes
G
PNI (–)
PNI (+)
P < 0.001
Relative FC
H
CK19|DAPI
TUJ1|DAPI
MERGE
With severe PNI
Without severe PNI
I
MERGE
PNI (+)
PNI (–)
OGA
OGA
***
Integrated option density
J
OGA-positive expression (%)
PNI (+) N = 39
OGA low 12.82%
OGA medium 46.15%
OGA high 41.03%
K
Strata
OGA medium
OGA high
HR = 3.13 (1.49–6.56)
P < 0.001
Survival probability (%)
Follow-up time (months)
L
Medium and high OGA-positive expression (%)
0/27
10/18
13/15
5/6
PNI (–)
Mild infiltration
Moderate infiltration
Severe infiltration

oxidative phosphorylation, and amino acid metabolism. All test compounds were initially aliquoted into 96-well plates in DMSO solution and administered at 10 μmol/L final concentration. Following EV pretreatment, neuronal cells were plated into the compound-containing wells (100 μL medium/well) and cocultured for 24 hours. Two control groups were included: untreated neurons and EV-treated neurons with DMSO only. Cell viability was used as the screening readout.

Primary bone marrow–derived macrophage isolation

Primary bone marrow–derived macrophages (BMDM) were harvested from 6- to 8-week-old healthy male C57BL/6J mice (RRID: IMSR_JAX:000664). After CO_2 anesthesia and cervical dislocation, femurs and tibiae were aseptically dissected for subsequent cell isolation. The bone marrow cavities were opened at both ends, and BMDMs were flushed out using PBS supplemented with 2% FBS through a syringe. Following collection, the flushed suspension was centrifuged at 300 × *g* for 5 minutes. The resulting pellet was resuspended, filtered to eliminate tissue debris, and counted. Cells were then seeded in nonadherent dishes at 1×10^6 cells/mL in complete DMEM with 10% FBS, 1% penicillin–streptomycin, and 20 ng/mL recombinant mouse macrophage colony–stimulating factor (M-CSF) to drive macrophage differentiation. Cells were cultured at 37°C under 5% CO_2 with periodic medium replacement (50% volume every 48 hours). Following 7 days of M-CSF induction, the adherent population exhibited characteristic macrophage morphology, including polygonal cellular architecture. Differentiated macrophages were collected on day 7 for downstream applications.

Real-time imaging of neuronal and BMDM cell death using SYTOX Green

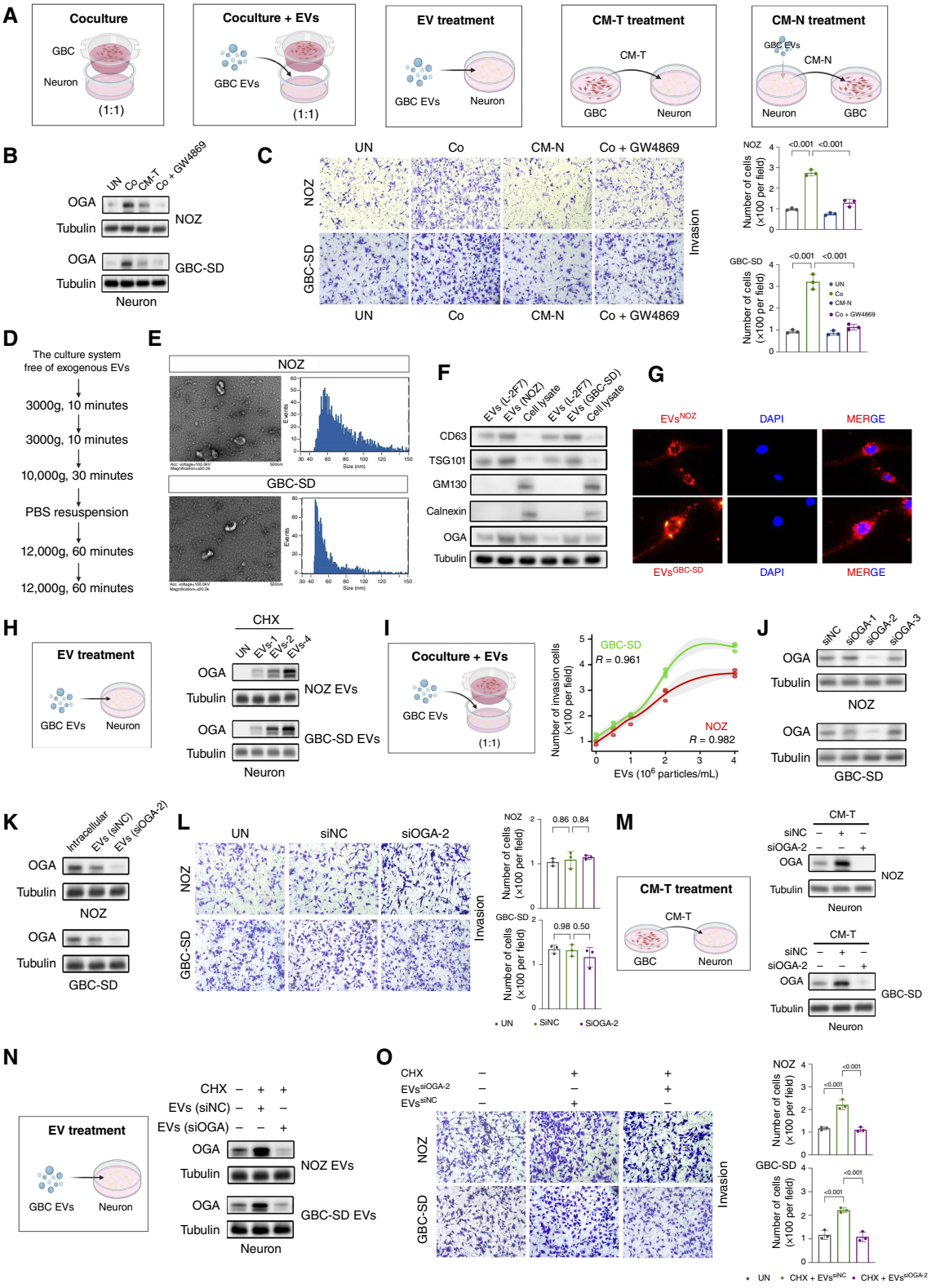
Neurons were cultured following standard protocols, including untreated and genetically modified (e.g., site-mutated or siRNA-transfected) groups. Cells were plated in 96-well plates at densities ranging from 6,000 to 10,000 cells per well (Corning, 3596). After stabilization, cells were subjected to various treatments, such as EV exposure (e.g., from gallbladder cancer cells), pharmacologic intervention [e.g., necrostatin-1 (Nec-1), glucosamine, or OGA inhibitor thiamet G (TMG)], and appropriate negative (PBS or DMSO) and positive controls (Triton X-100). SYTOX Green dye (Thermo Fisher Scientific, S7020), which penetrates only membrane-compromised cells and fluoresces upon nucleic acid binding, was added at 1:10 dilution. Readings were acquired with a BioTek Synergy H1 instrument housed within an environmentally controlled chamber providing precise regulation of temperature and CO_2 levels. Time-lapse images were acquired every 30 minutes for 24 hours. Cell death was quantified based on SYTOX-positive nuclei counts or fluorescence intensity, expressed as either "number of dead cells per field" or "percentage of dead cells." Six biological replicates were used per group. The results were presented as the mean ± SD and used for statistical comparisons. For BMDM cell death monitoring, the same protocol was applied. To construct RIPK1-dependent and -independent cell death models, the following stimuli were used: TNFα (10 ng/mL) + Smac mimetic BV6 (2 μmol/L; ref. 24); TNFα + 5Z-7-oxozeaenol (200 nmol/L; ref. 25); TNFα + BV6 + z-VAD-FMK Z-VAD-FMK (ZVAD; 20 μmol/L; ref. 26); TNFα + 5Z-7-oxozeaenol + z-VAD-FMK; lipopolysaccharide (LPS; 200 ng/mL) + 5Z-7-oxozeaenol (27); *Yersinia* [multiplicity of infection (MOI = 40; ref. 28)]; *Salmonella* (MOI = 100; ref. 29); and LPS + nigericin (10 μmol/L; ref. 29). For metabolic starvation models, glucose-free media were used 5 hours prior to stimulation. Pretreatments (e.g., TNFα, LPS, and TMG) were administered 1 hour before costimulation. Information on drugs was provided in Supplementary Table S3.

LDH release assay

To assess membrane integrity and cell damage in neurons and BMDMs, LDH release was quantified using a commercial LDH Assay Kit (MedChemExpress, HY-K1090). For experimental analysis, cells were plated in 96-well plates at densities of 6,000 to 10,000 cells per well and exposed to different treatment conditions. These interventions included EVs, pharmaceutical compounds (such as Nec-1, TMG, and GlcN), siRNA-mediated gene silencing, or coculture with tumor cells. Controls included untreated wells and a positive lysis control (Triton X-100) representing maximal LDH release. Following treatment, plates were centrifuged at 300 × *g* for 5 minutes, and 50 μL aliquots of supernatant were transferred to fresh plates. An equal volume of LDH reaction solution was added, mixed, and incubated protected from light for 30 minutes at room temperature. The reaction was terminated with stop solution (50 μL/well), and absorbance was read at 490 nm. Background absorbance (media only) was subtracted. LDH release was calculated

Figure 1.

Neuronal OGA increased in PNI of gallbladder cancer. **A,** H&E staining shows the histologic features of PNI in gallbladder cancer tissue. Left, a PNI-negative sample. Right, a PNI-positive sample. Top, low-magnification view (scale bar, 50 μm). Bottom, high-magnification view (scale bar, 20 μm). Red arrows, nerve bundles; green arrows, tumor cells surrounding the nerve. In PNI-positive samples, tumor cells are clearly seen infiltrating around and into the nerve bundles. **B,** Kaplan–Meier survival curves of gallbladder cancer patients with or without PNI. A total of 39 patients were included in the PNI-positive group, and 27 in the PNI-negative group. Shaded areas indicate the 95% CIs. **C,** Multivariate Cox regression analysis of OS in patients with gallbladder cancer. Red dots indicate statistically significant variables ($P < 0.05$), whereas blue dots indicate nonsignificant variables. TNM, tumor–node–metastasis. **D,** Single-cell clustering of gallbladder cancer tissue and intercellular communication between tumor epithelial cells and neurons. Top, Uniform Manifold Approximation and Projection (UMAP) dimensionality reduction plot of scRNA-seq data. Bottom, a cell–cell communication network between tumor epithelial cells and nerve-associated cells. **E,** Schematic overview of the laser-assisted proteomics analysis. A total of 22 gallbladder cancer tissue samples were collected, including 11 PNI-positive and 11 PNI-negative cases. Serial sections were subjected to H&E, IF, and IHC staining. Laser microdissection was used to precisely isolate the regions of interest for high-sensitivity mass spectrometry analysis, yielding the differential protein profiles from PNI regions. **F,** Volcano plot of differentially expressed proteins in PNI-positive vs. PNI-negative regions. **G,** Differential expression of OGA protein in PNI-positive and PNI-negative regions. **H,** Representative IF images of CK19 and TUJ1 staining in gallbladder cancer tissues from patients with or without severe PNI. CK19 marks tumor cells, whereas TUJ1 marks neuronal cells. Dotted lines, tumor boundaries. Scale bar, 50 μm. **I,** Colocalization and relative quantification of OGA expression in PNI regions using combined IF and IHC ($n = 12$ per group). Left, IF staining showing tumor cells (CK19+) and neurons (TUJ1+). Right, IHC staining and quantification of OGA expression. Scale bar, 50 μm. **J,** Distribution of OGA expression in neurons from 39 PNI-positive gallbladder cancer samples. **K,** Kaplan–Meier survival analysis comparing gallbladder cancer patients with high vs. medium neuronal OGA expression. **L,** Proportion of moderate-to-high OGA expression across different PNI grades. **E,** Created in BioRender. Zhao, J. (2025) https://BioRender.com/c6rntn4.


A
Coculture
GBC
Neuron
(1:1)
Coculture + EVs
GBC EVs
(1:1)
EV treatment
GBC EVs
Neuron
CM-T treatment
CM-T
GBC
Neuron
CM-N treatment
GBC EVs
CM-N
Neuron
GBC
B
UN
Co
CM-T
Co + GW4869
OGA
Tubulin
NOZ
GBC-SD
Neuron
C
UN
Co
CM-N
Co + GW4869
NOZ
GBC-SD
Invasion
Number of cells (×100 per field)
<0.001
D
The culture system free of exogenous EVs
3000g, 10 minutes
3000g, 10 minutes
10,000g, 30 minutes
PBS resuspension
12,000g, 60 minutes
12,000g, 60 minutes
E
NOZ
GBC-SD
Events
Size (nm)
F
EVs (L-2F7)
EVs (NOZ)
Cell lysate
EVs (L-2F7)
EVs (GBC-SD)
Cell lysate
CD63
TSG101
GM130
Calnexin
OGA
Tubulin
G
EVsNOZ
DAPI
MERGE
EVsGBC-SD
DAPI
MERGE
H
EV treatment
GBC EVs
Neuron
CHX
UN
EVs-1
EVs-2
EVs-4
OGA
Tubulin
NOZ EVs
GBC-SD EVs
Neuron
I
Coculture + EVs
GBC EVs
(1:1)
GBC-SD
R = 0.961
NOZ
R = 0.982
Number of invasion cells (×100 per field)
EVs (10^6 particles/mL)
J
siNC
siOGA-1
siOGA-2
siOGA-3
OGA
Tubulin
NOZ
GBC-SD
K
Intracellular
EVs (siNC)
EVs (siOGA-2)
OGA
Tubulin
NOZ
GBC-SD
L
UN
siNC
siOGA-2
NOZ
GBC-SD
Invasion
Number of cells (×100 per field)
0.86
0.84
0.98
0.50
UN
SiNC
SiOGA-2
M
CM-T treatment
CM-T
GBC
Neuron
CM-T
siNC
siOGA-2
OGA
Tubulin
NOZ
Neuron
GBC-SD
N
EV treatment
GBC EVs
Neuron
CHX
EVs (siNC)
EVs (siOGA)
OGA
Tubulin
NOZ EVs
GBC-SD EVs
Neuron
O
CHX
EVssiOGA-2
EVssiNC
NOZ
GBC-SD
Invasion
Number of cells (×100 per field)
UN
CHX + EVssiNC
CHX + EVssiOGA-2

using the following formula: LDH release (%) = [(OD490 sample–OD490 background)/(OD490 max–OD490 background)] × 100. All experimental data represent three or more independent replicates and are presented as the mean ± SD.

Structural modeling and docking analysis

To explore potential interactions between OGA and RIPK1, protein–protein docking and structural modeling were performed. The 3D structures of OGA and RIPK1 were sourced primarily from the RCSB Protein Data Bank, supplemented by predictions from the AlphaFold Database in the absence of high-resolution experimental structures. Structures were preprocessed using PyMOL (RRID: SCR_000305) or UCSF ChimeraX (RRID: SCR_015872), including chain renaming, residue renumbering, and removal of nonprotein molecules (e.g., ligands, ions, and water). Proteins were color-coded, and preliminary interface mapping was performed. Interface analysis was conducted using PDBePISA and PDBsum to identify interface area, hydrogen bonds, hydrophobic interactions, and electrostatic contacts. Protein–protein docking was performed using HADDOCK 2.4 (RRID: SCR_019091) and ClusPro online servers (RRID: SCR_018248), with active residues defined based on interface prediction. The best-scoring complexes (based on lowest binding energy and best clustering score) were visualized in PyMOL. These *in silico* findings provided a theoretical basis for subsequent experimental validation.

Construction of RIPK1 point mutants

RIPK1 point mutants at serine residues S166A, S331A, S440A, and S669A were generated by overlapping PCR mutagenesis. The human RIPK1 open reading frame was used as the template. Mutation-specific primers containing site-directed base substitutions with 15 to 20 bp complementary overlaps were designed for each site. Site-directed mutagenesis of RIPK1 was performed by two-step overlapping PCR. The fused product was digested and inserted into pcDNA3.1-FLAG, followed by DH5α transformation and Sanger sequencing confirmation of successful mutation. The validated constructs (S166A, S331A, S440A, and S669A) were subsequently used for transfection and functional assays.

Co-IP assay

To empirically validate the physical association between OGA and RIPK1 (including its mutant variants), co-IP was conducted. HEK293T cells (RRID: CVCL_0063) were transfected with expression constructs encoding FLAG-tagged wild-type (WT) RIPK1, its phosphosite mutants (S331A, S440A, and S669A), and HA-tagged OGA using Lipofectamine 3000 reagent (Thermo Fisher Scientific, L3000015). Following 48-hour transfection, cells were harvested and lysed using RIPA buffer supplemented with protease and phosphatase inhibitors. The clarified supernatants were then collected for subsequent IP assays. Protein lysates (500–800 μg) were subjected to IP with preequilibrated anti-FLAG (MedChemEexpress, HY-K0207) or anti-HA (MedChemExpress, HY-K0201) magnetic beads during an overnight incubation at 4°C with gentle agitation. After washing the complexes with cold PBS, proteins were eluted in SDS buffer via boiling, resolved by SDS-PAGE, and analyzed by immunoblotting to identify binding partners.

AAV serotype 9–mediated neuronal RIPK1 knockout

To achieve neuron-specific knockout of RIPK1, a CRISPR–Cas9 system-based AAV serotype 9 (AAV9) vector was constructed, following the sciatic nerve delivery protocol described by Mette Richner and colleagues (24). Gene delivery was performed using the sciatic nerve direct immersion method. Following isoflurane anesthesia, the right sciatic nerve bifurcation in 5-week-old female BALB/c nude mice was exposed through careful dissection to create the surgical field. After blunt dissection of muscle based on anatomic landmarks, 10 μL of thawed AAV9 virus (2.8×10^{10} vg, CMV:eGFP expression cassette) was slowly applied to the nerve surface without direct puncture. The muscle layer was gently closed, and the skin was sealed with medical adhesive. NSAIDs were administered subcutaneously for analgesia, and animals were monitored postoperatively before returning to specific pathogen-free housing. At the experimental endpoint (3–6 weeks after injection), nude mice were euthanized, and relevant tissues, including sciatic nerve, DRG, spinal cord, and biceps femoris muscle, were harvested for subsequent examination.

ELISA for damage-associated molecular pattern quantification

To measure the simultaneous release of multiple damage-associated molecular patterns (DAMP) from neuronal cultures

Figure 2.

Gallbladder cancer–derived EVs increase neuronal OGA. **A,** Schematic diagram of the Transwell-based coculture system between gallbladder cancer cells and neurons, comprising five experimental conditions: (i) Coculture: Noncontact coculture of gallbladder cancer and neuronal cells in a 1:1 ratio (gallbladder cancer in the upper chamber and neurons in the lower chamber); (ii) Coculture + EVs: Same as above, with additional gallbladder cancer–derived EVs added to the lower chamber; (iii) EV treatment: Gallbladder cancer–derived EVs were directly added to neurons; (iv) CM-T treatment: Neurons were treated with NOZ-CM; (v) CM-N treatment: Gallbladder cancer cells were treated with CM-N- collected after EV exposure. **B,** WB analysis of OGA expression in neurons under the indicated conditions. UN, untreated neurons; Co, neurons cocultured with gallbladder cancer cells; CM-T, neurons treated with NOZ-CM; Co + GW4869, coculture with addition of EV inhibitor GW4869 (10 μmol/L). **C,** Representative images (left) and quantitative analysis (right) of gallbladder cancer cell invasion toward neurons in the Transwell assay under indicated conditions. **D** and **E,** Schematic overview of the EV isolation workflow from gallbladder cancer cells. TEM image of gallbladder cancer–derived EVs (left) and NTA-based size distribution (right). Scale bar, 50 nm. **F,** WB of EV markers and OGA protein in EVs derived from gallbladder cancer cells. CD63 and TSG101 were routinely used as positive EV markers, whereas the intracellular proteins GM130 and calnexin served as negative controls. **G,** Representative fluorescence images of neurons treated with DiO-labeled EVs. **H,** WB showing the presence of exogenous OGA protein in neurons following treatment with gallbladder cancer–derived EVs. EVs were categorized into three concentrations: EV-1 (0.5×10^6 particles/mL), EV-2 (1×10^6 particles/mL), and EV-4 (2×10^6 particles/mL). **I,** Schematic of neuroinvasion assay following EV treatment. Tumor-derived EVs were added to the coculture system, and the invasive ability of gallbladder cancer cells toward neurons was assessed. **J** and **K,** WB analysis of OGA knockdown in gallbladder cancer cells and corresponding EVs. **J,** OGA expression in gallbladder cancer cells after siRNA transfection. **K,** OGA expression in EVs derived from gallbladder cancer cells transfected with siOGA-2. **L,** Representative images (left) and quantification (right) of gallbladder cancer cell invasion toward neurons under indicated siRNA. **M,** WB of OGA expression in neurons after treatment with CM-T. **N,** WB of OGA expression in neurons after treatment with gallbladder cancer–derived EVs. **O,** Representative image (right) and quantification (left) of gallbladder cancer cell invasion toward neurons in the Transwell system under the indicated conditions. Data are presented as the mean ± SD. Statistical comparisons were performed using one-way ANOVA with the Tukey *post hoc* test (**C**, **L**, and **O**). **A**, **H**, **I**, **M**, and **N,** Created in BioRender. Zhao, J. (2025) https://BioRender.com/c6rntn4.

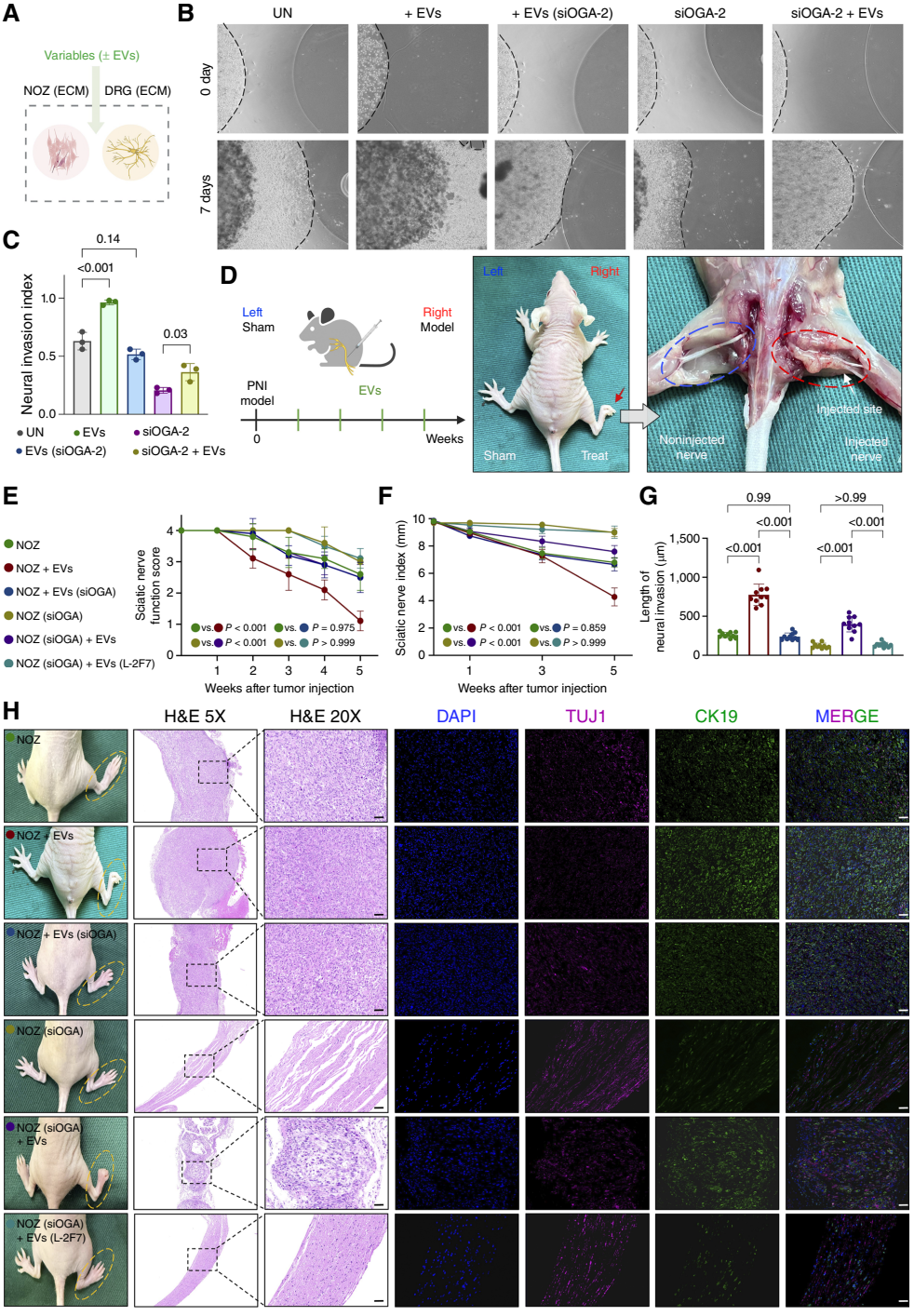


Figure 3.
Gallbladder cancer EVs package OGA to promote PNI. **A,** Schematic illustration of the 3D coculture model, showing NOZ cells (left) and DRG (right). **B,** Representative image of the 3D coculture of murine DRG with NOZ cells under the indicated treatments. UN, untreated. **C,** Quantification of the neural invasion index in the 3D coculture model. **D,** Schematic of the sciatic nerve invasion model. NOZ cells were directly injected into the sciatic nerves of nude mice ($n = 10$ mice per group). The left hind limb was designated as the sham-operated control (simple exposure of the sciatic nerve without further manipulation), whereas the right hind limb underwent full surgical exposure and sciatic nerve modeling. **E** and **F,** Sciatic nerve function was performed weekly by calculating the sciatic nerve function score (**E**) and sciatic nerve index (**F**). Solid circles of distinct colors denote the different experimental groups. **G,** Quantification of the neural invasion length. **H,** Lower-limb neurologic status, H&E staining, and IF images of sciatic nerve invasion. TUJ1 was used as a neuronal marker, whereas CK19 was used as a tumor marker. Dotted lines delineate tumor boundaries. Scale bars, 50 μm. Data are presented as the mean ± SD. Statistical comparisons were performed using one-way ANOVA with the Tukey *post hoc* test (**C** and **E–G**). **A** and **D,** Created in BioRender. Zhao, J. (2025) https://BioRender.com/c6rntn4.

after treatment with gallbladder cancer–derived EVs, commercial ELISA kits were used for each target following the protocols supplied by the manufacturers: human IL33 (cat. #ab223865, Abcam, RRID: AB_3712870), HMGB1 (EEL047, Invitrogen, Thermo Fisher Scientific, RRID: AB_3712872), HSP90 (cat. #ab320052, Abcam, RRID: AB_3712873), histones (Cloud-Clone Corp, cat. #USEA285Mi, RRID: AB_3712874), S100A8/9 (cat. #ab267628, Abcam, RRID: AB_3712875), and HSP70 (cat. #ab133060, Abcam, RRID: AB_3712876). After treatment with EVs, neuronal supernatants were collected at indicated time points and processed by centrifugation to remove cellular debris. Cleared samples were either used promptly or preserved at −80°C in aliquots while restricting freeze–thaw cycles to two or fewer. ELISA measurements were conducted in triplicate using sample aliquots and standard curves. Following sequential antibody and substrate incubations, absorbance values were recorded.

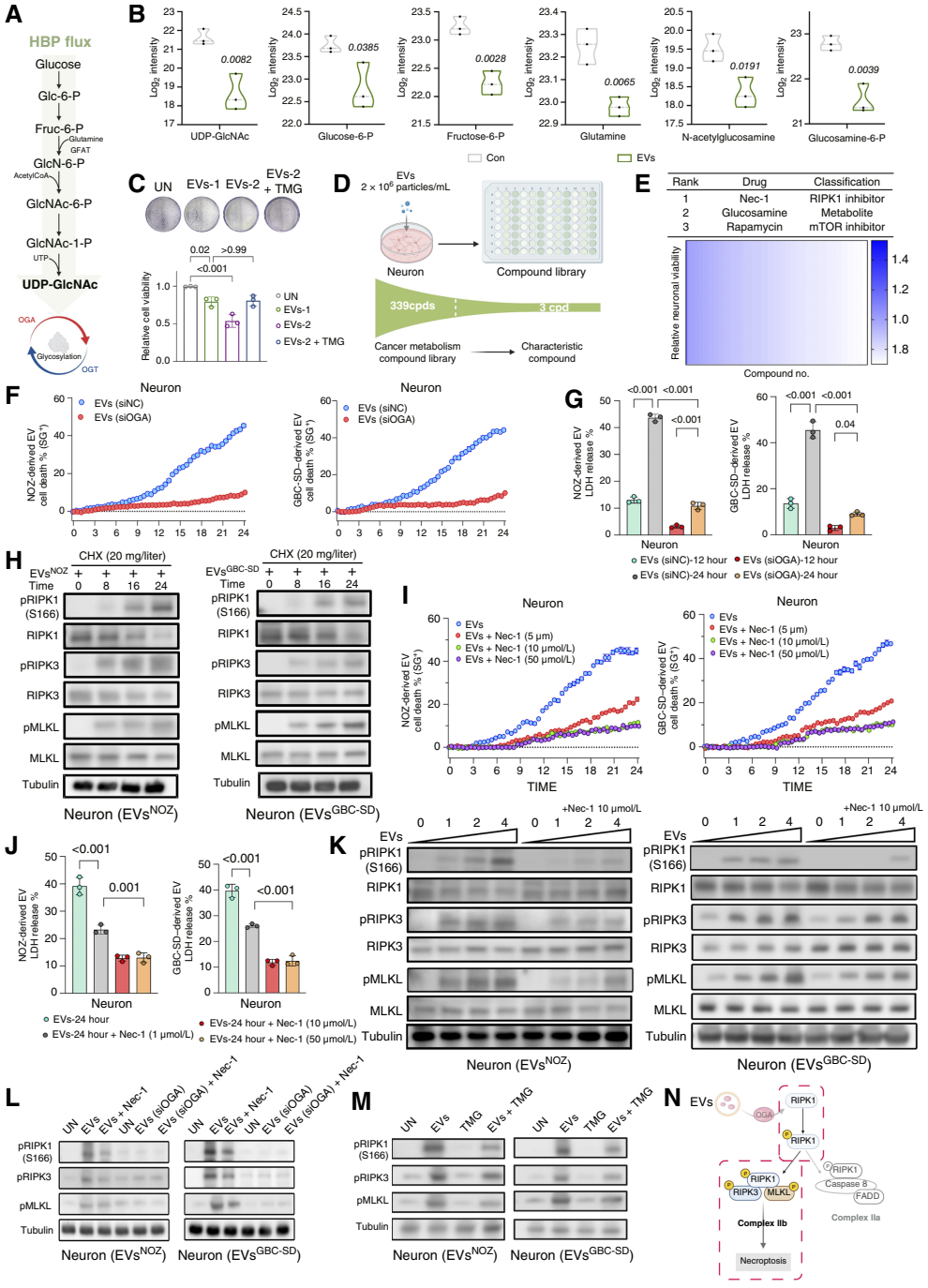
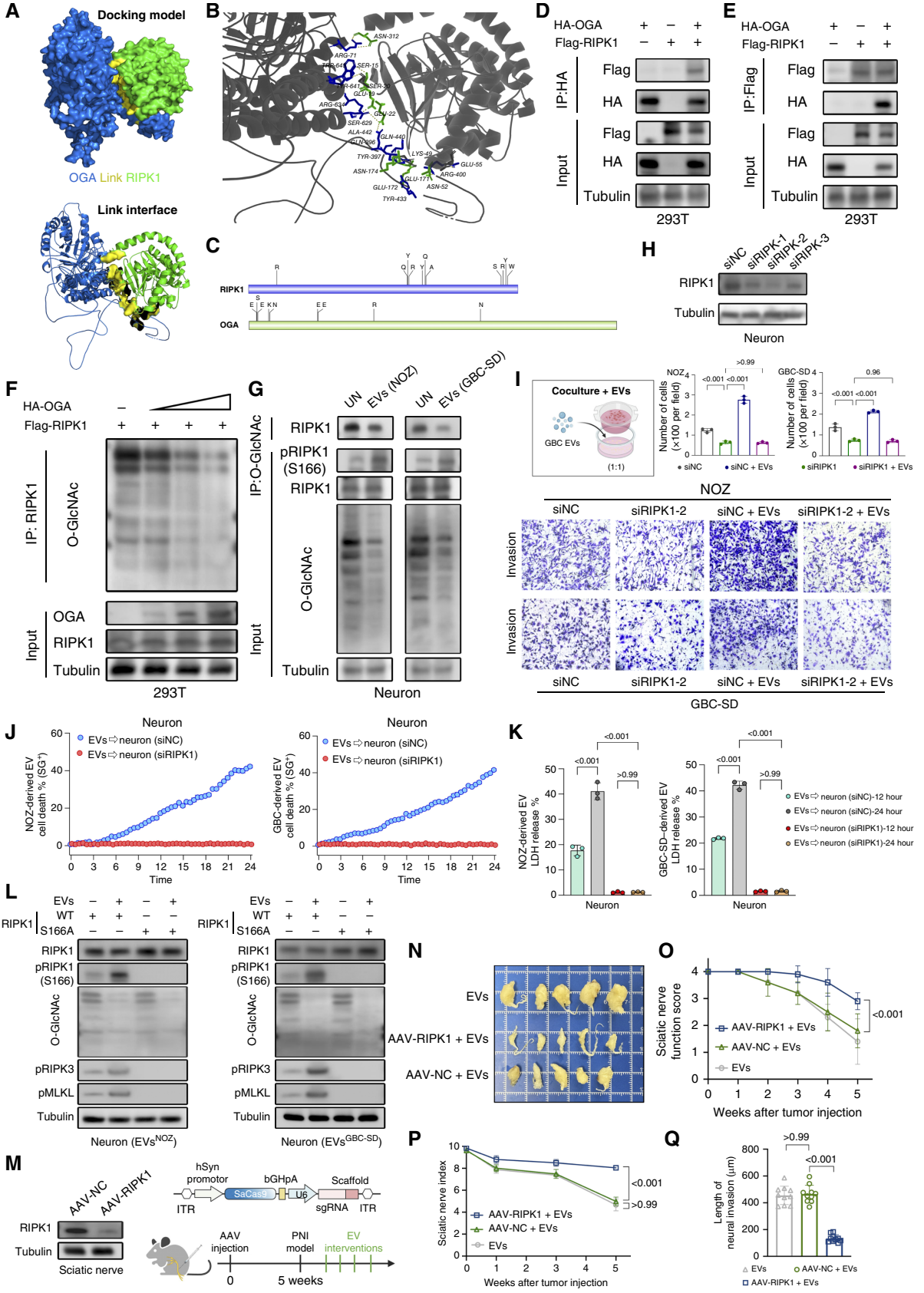


Figure 4.

Exosomal OGA induces RIPK1-dependent necroptosis in neuron. **A,** Schematic illustration of the HBP and glycosylation-related signaling. **B,** Metabolomic profiling of neurons after treatment with gallbladder cancer–derived EVs. **C,** Representative images of crystal violet staining (top) and quantitative analysis of cell viability (bottom) in neurons treated under the indicated conditions. **D,** Workflow of simulated treatment using a cancer metabolism–related compound library. **E,** Ranking of protective effects of metabolism-related compounds following EV-induced neuronal cell death. Heatmap indicates the impact of each compound on neuronal survival. Nec-1, glucosamine, and rapamycin showed the top three protective effects. **F** and **G,** EV-induced neuronal cell death was assessed by SYTOX Green positivity (**F**) and LDH release (**G**). **H,** WB of phosphorylated RIPK1, RIPK3, and MLKL in neurons treated as indicated. **I** and **J,** Neurons were pretreated with Nec-1 for 1 hour, followed by treatment with gallbladder cancer–derived EVs for the indicated durations. Necroptosis was measured by SYTOX Green positivity (**I**) and LDH release assay (**J**). **K,** WB analysis of phosphorylated RIPK1, RIPK3, and MLKL in neurons following cycloheximide (CHX) pretreatment and subsequent EV exposure. **L** and **M,** WB of the expression of phosphorylated RIPK1, RIPK3, and MLKL in neurons under additional indicated conditions. **N,** Schematic diagram illustrating the activation of complex IIb during necroptosis. Data are presented as the mean ± SD. Statistical comparisons were performed using unpaired Student *t* test (**B**) and one-way ANOVA with the Tukey *post hoc* test (**C**, **G**, and **J**). UN, untreated. **A**, **D**, and **N,** Created in BioRender. Zhao, J. (2025) https://BioRender.com/c6rntn4.


A
Docking model
OGA Link RIPK1
Link interface
B
C
RIPK1
OGA
D
HA-OGA
Flag-RIPK1
IP:HA
Flag
HA
Input
Flag
HA
Tubulin
293T
E
HA-OGA
Flag-RIPK1
IP:Flag
Flag
HA
Input
Flag
HA
Tubulin
293T
H
siNC
siRIPK-1
siRIPK-2
siRIPK-3
RIPK1
Tubulin
Neuron
F
HA-OGA
Flag-RIPK1
IP: RIPK1
O-GlcNAc
Input
OGA
RIPK1
Tubulin
293T
G
UN
EVs (NOZ)
UN
EVs (GBC-SD)
IP:O-GlcNAc
RIPK1
pRIPK1 (S166)
RIPK1
O-GlcNAc
Input
Tubulin
Neuron
I
Coculture + EVs
GBC EVs
(1:1)
NOZ
GBC-SD
Number of cells (×100 per field)
siNC
siNC + EVs
siRIPK1
siRIPK1 + EVs
NOZ
siNC
siRIPK1-2
siNC + EVs
siRIPK1-2 + EVs
Invasion
GBC-SD
J
Neuron
EVs⇨neuron (siNC)
EVs⇨neuron (siRIPK1)
NOZ-derived EV cell death % (SG+)
GBC-derived EV cell death % (SG+)
Time
K
NOZ-derived EV LDH release %
GBC-SD-derived EV LDH release %
Neuron
EVs⇨neuron (siNC)-12 hour
EVs⇨neuron (siNC)-24 hour
EVs⇨neuron (siRIPK1)-12 hour
EVs⇨neuron (siRIPK1)-24 hour
L
EVs
RIPK1
WT
S166A
RIPK1
pRIPK1 (S166)
O-GlcNAc
pRIPK3
pMLKL
Tubulin
Neuron (EVsNOZ)
Neuron (EVsGBC-SD)
M
AAV-NC
AAV-RIPK1
RIPK1
Tubulin
Sciatic nerve
hSyn promotor
bGHpA
Scaffold
SaCas9
U6
sgRNA
ITR
AAV injection
PNI model
EV interventions
0
5 weeks
N
EVs
AAV-RIPK1 + EVs
AAV-NC + EVs
O
Sciatic nerve function score
AAV-RIPK1 + EVs
AAV-NC + EVs
EVs
Weeks after tumor injection
P
Sciatic nerve index
AAV-RIPK1 + EVs
AAV-NC + EVs
EVs
Weeks after tumor injection
Q
Length of neural invasion (μm)
EVs
AAV-NC + EVs
AAV-RIPK1 + EVs

HMGB1 receptor inhibitor screening

To identify potential inhibitors of the HMGB1 signaling axis, three receptor-targeting small molecules were evaluated in a neuronal–tumor cell coculture system after EV treatment. After establishing coculture, the following inhibitors were added to the upper chamber: MMG-11 (10 μmol/L), TLR4-IN-C34 (10 μmol/L), and FPS-ZM1 (10 μmol/L). For experimental use, all compounds were formulated as 10 mmol/L DMSO stock solutions, with the final 10 μmol/L concentration achieved by dilution in the assay medium. After addition to the coculture system, transwell invasion assays were performed to assess tumor cell invasion toward the neuron compartment. Invasive cells were quantified under a microscope across five random fields per membrane.

Drug dose–response and cytotoxicity assay (IC_{50} value determination)

To determine the inhibitory effect of FPS-ZM1, gemcitabine, and their combination on gallbladder cancer cell proliferation, CCK8 assays were performed, and IC_{50} values were calculated. Cells were treated with a gradient of drug concentrations for 48 hours. Cell viability was quantified by measuring absorbance at 450 nm, and the IC_{50} was derived through nonlinear regression analysis in GraphPad Prism. CI values were calculated to evaluate synergistic effects.

Serum biochemical analysis and drug organ toxicity assessment

To evaluate the *in vivo* hepatorenal toxicity profiles of FPS-ZM1, terminal blood samples were obtained from anesthetized mice via cardiac puncture. After a 30-minute clotting period at room temperature, samples were centrifuged at 3,000 × *g* for 10 minutes to obtain serum for subsequent analysis. Serum biochemical indices were measured using commercial kits: BUN (MeilunBio, ml076479), aspartate aminotransferase (Abcam, ab105135), and alanine aminotransferase (Abcam, ab105134). Optical density readings were recorded at the specified wavelengths using a microplate reader. All samples were run in technical replicates, and experiments were performed at least three times. Values represent the mean ± SD. Significant differences were determined via one-way ANOVA with the Tukey test for multiple comparisons. To evaluate systemic toxicity of drug treatment, nude mice were euthanized after the final intervention. Multiple organs (heart, liver, spleen, lung, and kidney) were harvested. These tissue samples were then prepared for H&E staining using the established method to examine possible histopathologic damage.

Combination treatment and synergy analysis

To evaluate the combinatorial effects of FPS-ZM1 and gemcitabine, NOZ and GBC-SD cells were exposed to concentration gradients of both agents arranged in a fixed-ratio design. Cells plated in 96-well plates received concurrent treatment with FPS-ZM1 and gemcitabine for 72 hours. Viability was quantified by CCK8 assay, and drug interaction was analyzed via the SynergyFinder platform (https://synergyfinder.fimm.fi) using the zero interaction potency model. Synergy scores were interpreted as follows: >10 (synergistic), −10 to 10 (additive), and < −10 (antagonistic). The results were visualized using 2D synergy heatmaps and 3D response surface plots. All synergy scores and *P* values were automatically generated by the SynergyFinder platform.

Cross-species protein sequence alignment

To examine the evolutionary conservation of OGA and RIPK1 across species, we conducted multiple sequence alignments of human and mouse orthologs using Clustal Omega (https://www.ebi.ac.uk/Tools/msa/clustalo/). The complete protein sequences were obtained from UniProt using the following accession numbers: human OGA (Q96BI9), mouse OGA (Q8C0V7), human RIPK1 (Q13546), and mouse RIPK1 (Q64373). Sequences were aligned using default settings, and the results were visualized using Jalview (RRID: SCR_006459). In the alignment output, fully conserved residues were marked in dark blue, similar residues in light blue, and chemically distinct residues were color-coded by their physicochemical properties.

Statistical analysis

All analyses were conducted with SPSS version 13.0 and GraphPad Prism version 10.0. Continuous variables are expressed as the mean ± SD. Two-group comparisons were performed using an unpaired two-tailed Student *t* test. Three or more groups were compared by one-way ANOVA with the Tukey *post hoc* test. Data were checked for normality (Shapiro–Wilk) and homoscedasticity (Levene test) before being analyzed by one-way ANOVA followed by the Tukey multiple comparisons test. Significance was set at $\alpha = 0.05$. Survival curves were constructed with the Kaplan–Meier method and compared by the log-rank test. Independent prognostic factors were identified with multivariate Cox proportional hazards regression. Variables retaining $P \leq 0.05$ indicate statistical significance. Statistical parameters, including the number of mice, number of replicates, and statistical tests used, as well as *P* values, are indicated in each figure legend.

Figure 5.

OGA inhibited glycosylation and promoted phosphorylation of RIPK1. **A,** Structural modeling of the OGA–RIPK1 interaction using the HDOCK platform. **B,** Visualization of the predicted amino acid interaction sites between OGA and RIPK1 in the 3D structural model. **C,** Schematic representation of the amino acid residues involved in the OGA–RIPK1 interaction in the 2D sequence model. **D** and **E,** Co-IP assay performed in HEK293T cells cotransfected with HA-tagged OGA and/or Flag-tagged RIPK1 plasmids confirmed their direct interaction. **F,** RIPK1 immunoprecipitates were analyzed by WB to assess O-GlcNAcylation levels in HEK293T. **G,** Endogenous co-IP using anti-RIPK1 antibody confirmed the direct interaction between OGA and RIPK1 in neurons treated with gallbladder cancer–derived EVs. **H,** WB validation of siRNA-mediated RIPK1 knockdown in neurons. **I–K,** Neurons were transfected with siRNA to knock down RIPK1 expression and subjected to subsequent functional assays. **I,** Quantification (top) and representative images (bottom) of gallbladder cancer cell invasion toward neurons in the Transwell assay under indicated conditions. Neuronal cell death induced by gallbladder cancer–derived EVs was assessed by SYTOX Green positivity (**J**) and LDH release assay (**K**). **L,** WB of RIPK1, pRIPK1 (S166), pRIPK3, and pMLKL in neurons following EV treatment. **M,** Top, schematic workflow of the AAV-RIPK1 vector design; bottom left, WB of RIPK1 expression in neurons after AAV-RIPK1 transduction; and bottom right, schematic workflow for model construction. **N,** Representative image of gallbladder cancer–induced sciatic nerve invasion *in vivo* model under the indicated treatments. **O** and **P,** Sciatic nerve function was performed weekly by calculating the sciatic nerve function score (**O**) and sciatic nerve index ($n = 10$ mice per group; **P**). **Q,** Quantification of the length of neural invasion. Data are presented as the mean ± SD. Statistical comparisons were performed using one-way ANOVA with the Tukey *post hoc* test (**C** and **E–G**) and unpaired Student *t* test (**J**). **I** and **M,** Created in BioRender. Zhao, J. (2025) https://BioRender.com/c6rntn4.

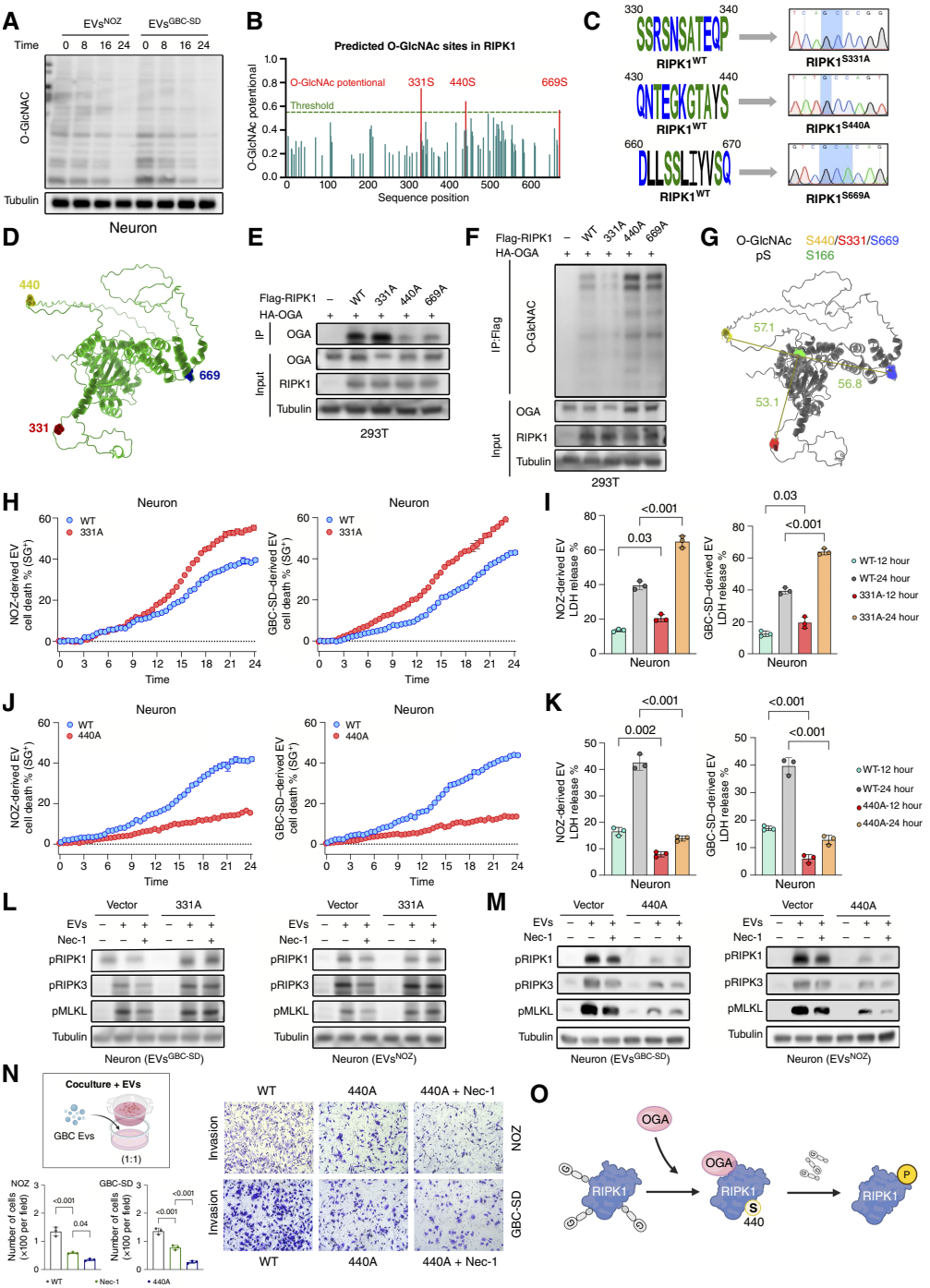


Figure 6.

Ser440 is a critical site of OGA-dependent O-GlcNAc site on RIPK1. **A,** WB showing that gallbladder cancer–derived EVs reduce the global O-GlcNAcylation level in neurons. **B,** Prediction of potential O-GlcNAcylation sites on RIPK1 using the online tool YinOYang. **C,** Construction and Sanger sequencing validation of RIPK1^{WT} and serine-to-alanine mutants: RIPK1^{S331A}, RIPK1^{S440A}, and RIPK1^{S669A}. The left shows the protein sequence, whereas the right panel shows the amino acid sequence. **D,** Structural schematic showing the spatial positions of serine residues 331, 440, and 669 on the RIPK1 protein. **E,** Co-IP assay assessing the ability of OGA to bind to RIPK1 in different RIPK1 mutants (WT, 331A, 440A, and 669A). **F,** IP assay evaluating changes in O-GlcNAc levels associated with each RIPK1 mutant. **G,** The spatial distances of the O-GlcNAcylation and phosphorylation sites on RIPK1. **H** and **I,** RIPK1^{S331A} or RIPK1^{WT} neurons were treated with gallbladder cancer–derived EVs, and neuronal necroptosis was assessed by SYTOX Green positivity (**H**) and LDH release (**I**). **J** and **K,** RIPK1^{S440A} or RIPK1^{WT} neurons were similarly treated with gallbladder cancer–derived EVs, and neuronal necroptosis was assessed by SYTOX (*Continued on the following page.*)

Results

Elevated neuronal OGA expression in gallbladder cancer PNI

Initially, a cohort of 39 PNI-positive patients and 27 PNI-negative patients with gallbladder cancer was categorized using H&E staining. In PNI-positive patients, tumor cells were observed to invade the perineural space or nerve sheath (**Fig. 1A**). Kaplan–Meier survival analysis revealed that PNI-positive patients had a significantly lower 5-year survival rate compared with PNI-negative patients (OR: 2.36–7.03, $P < 0.001$; **Fig. 1B**). Multivariate Cox regression analysis identified tumor size ≥3 cm, high/moderate grade, stages III to IV, and PNI positivity as independent factors for unfavorable prognosis ($P < 0.05$; **Fig. 1C**). Notably, single-cell sequencing of patients with gallbladder cancer showed more robust communication between tumor cells and neurons than with Schwann cells (**Fig. 1D**; Supplementary Fig. S1A). Subsequently, tumor tissues from 11 PNI-positive and 11 PNI-negative patients were selected to construct molecular maps of the neural microenvironment via laser microdissection and high-sensitivity mass spectrometry (**Fig. 1E**; Supplementary Fig. S1B). Proteomic analysis revealed a significant increase in OGA expression in PNI regions (**Fig. 1F** and **G**). The tumor-surrounding PNI region was confirmed by staining for the gallbladder cancer marker CK19 and the neural marker TUJ1. IF analysis showed CK19-positive tumor cells were clustered around TUJ1-positive neural markers (**Fig. 1H**). IHC combined with IF demonstrated a marked increase in neuronal OGA expression within PNI regions across 11 patients ($P < 0.001$, **Fig. 1I**). Patients were stratified based on OGA expression in PNI-positive cases. Among them, 34 patients (87.18%) exhibited medium-to-high OGA expression in neural regions, whereas 5 (12.82%) patients displayed low expression. All PNI-positive patients showed elevated OGA expression in neural areas (**Fig. 1J**). These results indicated that PNI-positive patients with high OGA expression had a poorer prognosis (**Fig. 1K**). Additionally, the extent of neural invasion was graded, revealing a direct correlation between the degree of PNI and the proportion of neurons with high OGA expression (**Fig. 1L**).

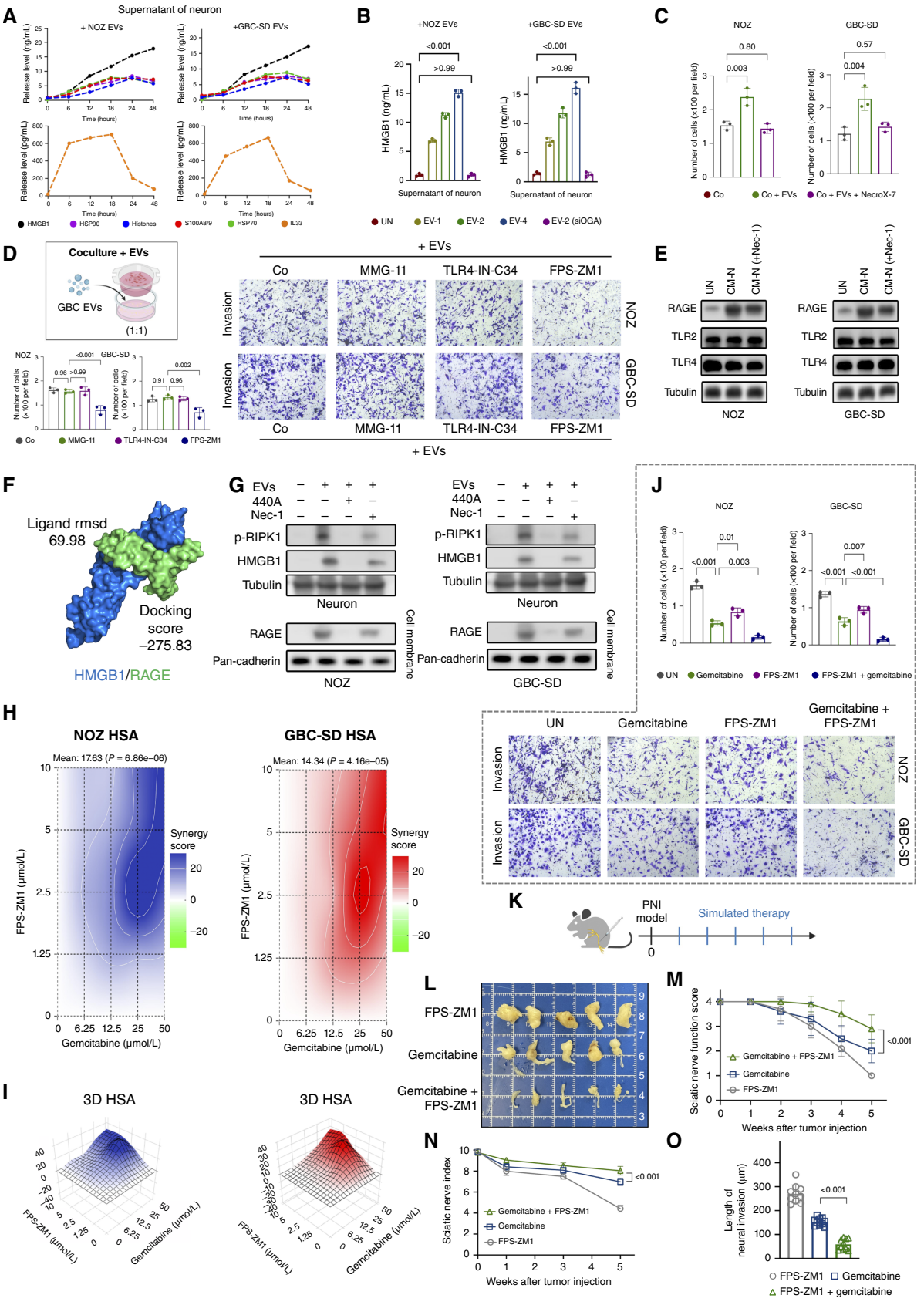
Gallbladder cancer–derived EVs mediate neuronal OGA upregulation

To investigate the mechanisms underlying OGA overexpression in neurons, gallbladder cancer cells were cocultured with neurons (**Fig. 2A**). In a noncontact coculture system, neuronal OGA levels were elevated following coculture or treatment with CM from NOZ cells (CM-T). This increase was attenuated when gallbladder cancer cells were pretreated with the EV inhibitor GW4869 (**Fig. 2B**). Coculture also enhanced the neurotropic invasion of gallbladder cancer cells toward neurons, whereas neuronal cell supernatant alone had no effect on gallbladder cancer cell invasion. Inhibition of gallbladder cancer–derived EVs significantly reduced the neural invasion capacity of gallbladder cancer cells (**Fig. 2C**). Given the fact that OGA is an intracellular protein rather than a secreted one, these findings suggested that the coculture medium might facilitate these changes through the EV pathway. To explore this hypothesis, EVs and other supernatants containing cytokines and metabolites were isolated from the culture media of two gallbladder cancer cell lines (NOZ and GBC-SD) using ultracentrifugation (**Fig. 2D**). NTA and TEM confirmed successful isolation and characterization of gallbladder cancer–derived EVs. TEM images revealed disc-shaped or cup-shaped EVs, and NTA quantification indicated that the size of gallbladder cancer–derived EVs were primarily ranged from 50 to 65 nm (**Fig. 2E**). WB analysis confirmed OGA cargo within EVs (**Fig. 2F**). To further test the hypothesis that neuronal OGA upregulation during PNI was mediated by gallbladder cancer–derived EVs, DiO-labeled EVs were coincubated with neurons to assess the delivery of tumor-derived EV delivery (**Fig. 2G**). After supplementation of neurons with gallbladder cancer–derived EVs, the increase in neuronal OGA was found to correlate with the quantity of EVs (**Fig. 2H**). Additionally, adding varying concentrations of EVs to the coculture system enhanced the invasive potential of gallbladder cancer cells (**Fig. 2I**). To validate that the increase in neuronal OGA was mediated by gallbladder cancer–derived EVs and assess changes in tumor invasiveness following coculture, OGA was knocked down in NOZ and GBC-SD cell lines, and EVs were extracted for OGA content analysis (**Fig. 2J** and **K**). The siRNA targeting OGA (siOGA-2) demonstrated the highest knockdown efficiency. Despite the knockdown, tumor cell invasiveness remained unaffected (**Fig. 2L**). WB analysis revealed that CM from siOGA-transfected tumor cells did not deliver OGA to neurons (**Fig. 2M**). Although EVs from control gallbladder cancer cells increased neuronal OGA, EVs derived from siOGA-transfected cells did not (**Fig. 2N**). The neurotropic invasion of tumor cells was reduced in the absence of OGA in EVs (**Fig. 2O**). These results collectively demonstrate that gallbladder cancer–derived EVs carrying OGA promote neurotropic invasion by transferring OGA to neurons.

Gallbladder cancer EVs package OGA to promote PNI

As *in vitro* coculture experiments have shown that tumor-derived EVs carrying OGA enhance the neurotropism of gallbladder cancer, we hypothesized that gallbladder cancer cells elevated neuronal OGA levels via EVs, thereby facilitating neurotropic invasion. This hypothesis was further validated using both *in vitro* and *in vivo* models. A 3D coculture model was used to evaluate how OGA within gallbladder cancer–derived EVs affects tumor cell invasion of DRG (**Fig. 3A**). Addition of EVs significantly enhanced the invasion of gallbladder cancer cell into DRG, although this effect was abolished when EVs lacked OGA. Reintroducing OGA via EVs rescued the invasive capacity of OGA-deficient tumor cells (**Fig. 3B** and **C**). Given the high protein homology of OGA between humans and mice (Supplementary Fig. S2), nude mouse sciatic nerve invasion models were utilized to further substantiate these findings. NOZ cells and OGA-deficient NOZ cells were injected into the sciatic nerve, followed by EV intervention (**Fig. 3D**). Sciatic nerve function index (SFI) revealed that supplementation with intact, OGA-containing EVs exacerbated tumor invasion of the sciatic nerve, whereas EVs lacking OGA failed to do so. Knockdown of OGA in the tumor cells attenuated the decline in the SFI, and this decline was restored by reintroducing functional OGA via EVs (**Fig. 3E**). Supplementation with either of the two OGA-deficient EV populations, derived from OGA-knockdown tumor cells or from normal gallbladder epithelial cells, elicited no statistically significant change in the SFI ($P > 0.85$; **Fig. 3E**). The length of gallbladder

(*Continued.*) Green positivity (**J**) and LDH release assay (**K**). **L** and **M,** WB of phosphorylated RIPK1, RIPK3, and MLKL in $RIPK1^{S331A}$ (**L**) or $RIPK1^{S440A}$ (**M**) following the indicated treatments. **N,** Representative images (right) and quantification (left) of gallbladder cancer cell invasion toward neurons in the Transwell assay under different RIPK1-mutant conditions. **O,** Schematic diagram indicating that S440 is a critical site of OGA-dependent O-GlcNAc site on RIPK1. Data are presented as the mean ± SD. Statistical comparisons were performed using one-way ANOVA with the Tukey *post hoc* test (**I**, **K**, and **O–Q**) and unpaired Student *t* test (**H** and **J**). **N** and **O,** Created in BioRender. Zhao, J. (2025) https://BioRender.com/c6rntn4.


A
Supernatant of neuron
+ NOZ EVs
+GBC-SD EVs
Release level (ng/mL)
Release level (pg/mL)
Time (hours)
HMGB1
HSP90
Histones
S100A8/9
HSP70
IL33
B
+NOZ EVs
+GBC-SD EVs
HMGB1 (ng/mL)
Supernatant of neuron
UN
EV-1
EV-2
EV-4
EV-2 (siOGA)
C
NOZ
GBC-SD
Number of cells (×100 per field)
Co
Co + EVs
Co + EVs + NecroX-7
D
Coculture + EVs
GBC EVs
(1:1)
+ EVs
Co
MMG-11
TLR4-IN-C34
FPS-ZM1
Invasion
NOZ
GBC-SD
E
UN
CM-N
CM-N (+Nec-1)
RAGE
TLR2
TLR4
Tubulin
F
Ligand rmsd
69.98
Docking
score
−275.83
HMGB1/RAGE
G
EVs
440A
Nec-1
p-RIPK1
HMGB1
Tubulin
Neuron
RAGE
Pan-cadherin
Cell membrane
NOZ
GBC-SD
J
NOZ
GBC-SD
Number of cells (×100 per field)
UN
Gemcitabine
FPS-ZM1
FPS-ZM1 + gemcitabine
H
NOZ HSA
GBC-SD HSA
Mean: 17.63 (P = 6.86e−06)
Mean: 14.34 (P = 4.16e−05)
Synergy score
FPS-ZM1 (μmol/L)
Gemcitabine (μmol/L)
I
3D HSA
K
PNI model
Simulated therapy
L
FPS-ZM1
Gemcitabine
Gemcitabine + FPS-ZM1
M
Sciatic nerve function score
Weeks after tumor injection
N
Sciatic nerve index
O
Length of neural invasion (μm)

cancer invasion along the sciatic nerve increased upon supplementation with intact tumor-derived EVs, whereas OGA-deficient EVs failed to elicit any such augmentation ($P > 0.99$; **Fig. 3E–G**). Mice treated with intact tumor-derived EVs exhibited more severe hind limb paralysis and markedly reduced paw width, whereas OGA-deficient tumor cells and supplementation with OGA-depleted EVs resulted in only moderate paralysis and intermediate paw width. IF staining showed that, compared with the OGA-deficient tumor group or the OGA-deficient EV group, mice receiving intact tumor-derived EVs displayed more extensive PNI, decreased neuronal marker TUJ1, and increased tumor marker CK19. Importantly, OGA-deficient tumor cells regained their capacity to invade nerves after receiving EV-delivered OGA (**Fig. 3H**). Collectively, these *in vitro* and *in vivo* data demonstrated that tumor-derived EVs carrying OGA markedly enhance PNI in gallbladder cancer.

Exosomal OGA induces RIPK1-dependent necroptosis in neurons

Protein glycosylation modification is a dynamic and reversible process regulated by OGT (O-GlcNAc transferase) and OGA (O-GlcNAc hydrolase; refs. 30, 31). The hexosamine biosynthesis pathway (HBP) is a critical metabolic pathway responsible for generating UDP-GlcNAc, the core substrate for various glycosylation modifications, including O-GlcNAc modification (**Fig. 4A**; ref. 32). To confirm that the increase in OGA originated from tumor cell EVs, metabolomics sequencing was performed on neurons treated with EVs (Supplementary Fig. S3A). After treatment with tumor-derived EVs, the overall metabolic flux in the HBP pathway of neurons was reduced (Supplementary Fig. S3B and S3C). Key metabolites, including glucose-6-P, fructose-6-P, glutamine, N-acetylglucosamine, glucosamine-6-P, and UDP-GlcNAc, were significantly decreased, indicating that exogenous OGA inhibits glycosylation modification in neurons (**Fig. 4B**). Neuronal viability also decreased following treatment with tumor-derived EVs, an effect that could be reversed by TMG (**Fig. 4C**). This suggests that the disruption of metabolic balance in neurons by exogenous OGA may contribute to reduced neuronal viability. Following EV-mediated transfer, OGA reduced neuronal O-GlcNAcylation, whereas OGT levels remained unchanged (Supplementary Fig. S3D). To further explore the mechanism underlying reduced neuronal viability, a metabolism-related drug library was used to screen for potential treatments following EV treatment (**Fig. 4D**). Nec-1, a RIPK1-targeting inhibitor, demonstrated the most significant neutralizing and rescuing effects against the EV-induced reduction in neuronal viability (**Fig. 4E**). Given that Nec-1 is an apoptosis-related inhibitor, neuronal cell death following EV treatment was further investigated. Tumor-derived EVs were found to induce neuronal cell death, as confirmed by real-time cell death kinetics assay and LDH release experiments (Supplementary Fig. S4A and S4B). LDH release indicated neuronal membrane damage after exposure to tumor-derived EVs, which decreased after treatment with Nec-1 (Supplementary Fig. S4C–S4F). EV-induced neuronal cell death was observed exclusively in the presence of OGA (**Fig. 4F** and **G**). EV-derived OGA induces neuronal cell death primarily through RIPK1 activation, whereas RIPK1 activation lead to the formation of protein complexes IIa and IIb, which mediated apoptosis and necroptosis, respectively (33). To distinguish between these pathways, cells were treated with the pan-caspase inhibitor ZVAD. ZVAD failed to neutralize or rescue EV-induced neuronal death, and no activation of complex IIa–associated proteins (caspase-8, cleaved caspase-8 p43, and cleaved caspase-8 p18) was observed after EV treatment (Supplementary Fig. S4G and S4H). This suggests that neuronal cell death was primarily mediated through the complex IIb pathway. We next examined the relationship between the RIPK1/RIPK3/MLKL pathway and complex IIb. After EV treatment, significant activation of this pathway was observed in neurons, and targeted inhibition of RIPK1 in neurons rescued EV-induced neuronal death (**Fig. 4H–J**). EVs activated the RIPK1/RIPK3/MLKL pathway in a dose-dependent manner, and Nec-1 suppressed this activation (**Fig. 4K**). EV-induced phosphorylation of RIPK1 in neurons occurred exclusively in the presence of OGA (**Fig. 4L**). Selected inhibition of neuronal OGA neutralized and rescued EV-induced neuronal death, also preventing the activation of the necroptotic complex IIb pathway in neurons (**Fig. 4M**; Supplementary Fig. S5A–S5C). Furthermore, supplementing GlcN to neurons directly increased glycosylation levels, decreased RIPK1 phosphorylation, and inhibited complex IIb formation, thereby rescuing neurons from EV-induced death (Supplementary Fig. S5D–S5H). To validate the general role of OGA in regulating RIPK1 phosphorylation, we constructed eight distinct cell death models. TMG was used to directly inhibit intracellular OGA, whereas GlcN was used to modulate intracellular glycosylation levels, thereby indirectly suppress OGA function. This finding confirmed the critical role of OGA in regulating cell survival and death. In cell death models dependent on RIPK1 activation (T/O, T/S, T/S/Z, T/O/Z, LPS/O, and *Yersinia* infection), treatment with TMG significantly rescued cells from death (Supplementary Figs. S6A–S6F and S7A–S7F). Similarly, supplementation with GlcN or inhibition with Nec-1 also effectively mitigated cell death (Supplementary Figs. S7G–S7L and S8A–S8F). Notably, direct inhibition of intracellular OGA produced the most pronounced rescue effects. Conversely, in cell death models independent of RIPK1 (LPS/nigericin and *Salmonella* infection), neither direct inhibition of OGA nor GlcN supplementation significantly mitigate cell death (Supplementary Figs. S6G and S6H, S7M–S7P,

Figure 7.

DAMP HMGB1/RAGE axis promotes PNI. **A** and **B,** ELISA quantification of DAMP release in neuronal supernatants following the indicated treatments. **C,** Quantitative analysis of gallbladder cancer cell invasion in the Transwell system under the indicated treatment conditions. **D,** Quantification (left) and representative images (right) of gallbladder cancer cell invasion in the Transwell system with the indicated treatments. **E,** WB analysis of RAGE expression in gallbladder cancer cells under the indicated conditions. **F,** Structural modeling of the interaction between HMGB1 and RAGE using the HDOCK platform. **G,** WB analysis of components in the HMGB1–RAGE signaling axis under the indicated treatments. **H** and **I,** Evaluation of the synergistic antitumor effect of FPS-ZM1 in combination with gemcitabine. **J,** Quantification (top) and representative images (bottom) of gallbladder cancer cell invasion in the Transwell system following combination treatment. **K–O,** *In vivo* evaluation of the therapeutic efficacy of FPS-ZM1 combined with gemcitabine. **K,** Schematic overview of the experimental workflow. Sciatic nerve invasion model was established, followed by the administration of simulated therapies. **M** and **N,** Sciatic nerve function was performed weekly by calculating the sciatic nerve function score (**M**) and sciatic nerve index (**N**). **O,** Quantification of the neural invasion length. Data are presented as the mean ± SD. Statistical comparisons were performed using one-way ANOVA with the Tukey *post hoc* test (**B–D**, **J**, and **M–O**). Co, neurons cocultured with gallbladder cancer cells; UN, untreated. **D** and **K,** Created in BioRender. Zhao, J. (2025) https://BioRender.com/c6rntn4.

S8G and S8H). These findings indicated that OGA-mediated deglycosylation of RIPK1 enhanced its phosphorylation, thereby triggering necroptosis via the protein complex IIb pathway (**Fig. 4N**).

OGA inhibits glycosylation and promotes phosphorylation of RIPK1

To investigate whether OGA induces necroptosis by inhibiting RIPK1 glycosylation, we utilized the HDOCK software to predict the 3D interaction model of OGA and RIPK1 (**Fig. 5A**). The most probable docking regions and relevant amino acid residues were identified (**Fig. 5B**) and further visualized in a 2D model (**Fig. 5C**). In HEK293T cells, cotransfection with HA-tagged OGA and FLAG-tagged RIPK1 and subsequent IP experiment was performed to confirm their direct interaction (**Fig. 5D** and **E**). Cotransfection with FLAG-RIPK1 and HA-OGT demonstrated that OGA significantly reduced RIPK1 O-GlcNAcylation (**Fig. 5F**). Moreover, endogenous co-IP analysis in neurons revealed that OGA derived from EVs inhibited RIPK1 glycosylation while promoting its phosphorylation (**Fig. 5G**). These findings suggested that EVs derived from gallbladder cancer deliver OGA to neurons, thereby inhibiting the glycosylation of RIPK1. This inhibition subsequently enhanced the phosphorylation and activation of RIPK1, ultimately triggering neuronal necroptosis. In subsequent experiments, knockdown in neurons (**Fig. 5H**) effectively abrogated the enhanced invasion of neurons by EVs (**Fig. 5I**). Moreover, the induction of neuronal necroptosis by EVs was also prevented (**Fig. 5J** and **K**), thereby confirming that OGA-mediated inhibition of RIPK1 glycosylation promoted its phosphorylation and subsequently drives necroptosis in neurons. To establish that downstream RIPK1 signaling depends on phosphorylation following deglycosylation, we introduced the phospho-null S166A mutation into neuronal RIPK1 (Supplementary Fig. S9). Despite gallbladder cancer–derived EVs markedly lowering global neuronal O-GlcNAc levels, mutation of the critical phospho-acceptor site S166 blocked RIPK1 phosphorylation and consequently prevented activation of the RIPK3/MLKL cascade (**Fig. 5L**). Considering the high degree of conservation of RIPK1 between humans and mice (Supplementary Fig. S10), AAV9 was utilized to specifically target mouse sciatic nerves, resulting in reduce RIPK1 expression and a subsequent decrease in neuronal necroptosis (**Fig. 5M**). This reduction in necroptosis significantly impeded the enhanced neural invasion mediated by EVs (**Fig. 5N–Q**). These results demonstrated that targeting RIPK1 to inhibit neuronal necroptosis effectively mitigates PNI.

Ser440 is a critical site of OGA-dependent O-GlcNAc site on RIPK1

To verify that OGA promoted RIPK1 phosphorylation by inhibiting its glycosylation, we first evaluated the glycosylation levels in cells treated with EVs. Neurons treated with EVs containing OGA exhibited reduced O-GlcNAc levels (**Fig. 6A**). We then utilized the YinOYang online database to predict potential O-GlcNAc glycosylation sites on RIPK1, which identified Ser331, Ser440, and Ser669 as possible modification sites (**Fig. 6B**). Plasmids harboring mutations at these sites were generated, comprising WT RIPK1 ($RIPK1^{WT}$) and single-point mutants ($RIPK1^{S331A}$, $RIPK1^{S440A}$, and $RIPK1^{S669A}$), with their sequences confirmed via Sanger sequencing (**Fig. 6C**). The spatial locations of these glycosylation sites on RIPK1 are depicted in **Fig. 6D**. Notably, compared with $RIPK1^{WT}$ and other mutants, the interaction between RIPK1 and OGA was significantly weakened in the 440A mutant, although it was markedly enhanced in the 331A mutant (**Fig. 6E**). Following the 440A mutation, RIPK1 bound OGA less avidly and displayed a corresponding increase in O-GlcNAc signal. However, the 331A mutation had the opposite effect (**Fig. 6F**). These findings indicate that glycosylation at Ser 440 was a crucial for the interaction between RIPK1 and OGA. In the RIPK1 structure, the phosphorylation site S166 was positioned almost equidistant to the O-GlcNAcylation sites S331, S440, and S669 (**Fig. 6G**). To further elucidate the role of Ser440 in mediating OGA's inhibition of RIPK1 glycosylation and its subsequent phosphorylation activation, cell death and the complex IIb pathway were examined. In cell death assays, the $RIPK1^{S331A}$ mutation significantly enhanced EV-induced necroptosis (**Fig. 6H** and **I**), whereas the 440A mutation attenuated necroptosis (**Fig. 6J** and **K**). The 331A mutation enhanced RIPK1 phosphorylation and activated the complex IIb pathway, with the inhibitory effect of Nec-1 on necroptosis being significantly weaker in $RIPK1^{S331A}$ than in $RIPK1^{WT}$. This effect was not observed with the S440A mutation (**Fig. 6L** and **M**). These observations were consistent with the differential effects of OGA on glycosylation following point mutations. Coculture experiments revealed that the RIPK1-S440A mutation counteracted neurotropic invasion (**Fig. 6N**). Collectively, these findings underscored the critical role of Ser440 in OGA-mediated inhibition of RIPK1 glycosylation and subsequent promotion of its phosphorylation (**Fig. 6O**).

DAMP HMGB1/RAGE axis facilitates PNI in gallbladder cancer

Necroptosis was characterized by plasma membrane rupture and the extracellular release of DAMPs. ELISA quantification of canonical DAMPs revealed that HMGB1 was the most abundant and persistently released factor after EV-induced neuronal necroptosis (**Fig. 7A**). Neuronal HMGB1 release exhibited both time- and dose-dependent correlations with EVs. Exposure to EVs evoked a time- and dose-dependent increase in HMGB1 levels in neuronal supernatants (**Fig. 7B**). Inhibition of EVs release effectively suppressed HMGB1 secretion, indicating that EVs regulated its export (Supplementary Fig. S11A). To establish HMGB1 as the DAMP mediating neurotropism in gallbladder cancer, we treated cocultured system with the HMGB1 inhibitor NecroX-7. NecroX-7 significantly attenuated the invasion effect of EVs (**Fig. 7C**), demonstrating that HMGB1 release promoted neurotropism through receptor engagement on tumor cells.

To identify the downstream ligands of HMGB1, various inhibitors were tested. The results showed that the RAGE inhibitor FPS-ZM1 significantly reduced the invasion of gallbladder cancer cells, whereas inhibitors of TLR2 and TLR4 had no significant effect (**Fig. 7D**). Further validation confirmed RAGE activation in tumor cells (**Fig. 7E**). The RAGE–HMGB1 interaction, a well-established receptor–ligand pair, was widely implicated in tumorigenesis. Molecular docking further verified the high affinity between RAGE and HMGB1 (**Fig. 7F**). Following EV treatment, RIPK1 phosphorylation increased in neurons, which resulted in the release of HMGB1 as DAMPs and subsequent RAGE activation in tumor cells. Inhibition of necroptosis with the S440A mutation and Nec-1 reduced the release of HMGB1 (**Fig. 7G**). RAGE, a surface receptor on tumor cells, was targeted by the high-affinity inhibitor FPS-ZM1 (Supplementary Fig. S11B and S11C). In dual cell line experiments, FPS-ZM1 demonstrated strong synergy with gemcitabine, with HSA values exceeding 10 (**Fig. 7H** and **I**; Supplementary Fig. S11D–S11G). The combination of FPS-ZM1 and gemcitabine more effectively inhibited invasion than either agent alone (**Fig. 7J**). In a nude mouse model of neural invasion, combination therapy with FPS-ZM1 and gemcitabine provided superior inhibition of invasion

and reduced hind limb motor deficits (**Fig. 7K–O**). Serum and pathologic analyses showed no significant organ toxicity from FPS-ZM1 (Supplementary Fig. S11H–S11K).

Discussion

The concept of tumor as a systemic disease has gained wide acceptance, drawing considerable attention to the specific role of the nervous system in tumor progression. PNI is a common pathologic hallmark in gallbladder cancer, and it is significantly correlated with unfavorable outcomes, such as poor prognosis, high recurrence rates, and low survival rates (7–9, 34, 35). The interaction between cancer cells and nerves is crucial to the adverse biological behavior of PNI, which involves the activation or inhibition of various signaling pathways, including chemokines, interleukins, and nerve growth factors (17, 29, 30). These interactions trigger specific alterations within the perineural niche, thereby disrupting normal nerve function and facilitating cancer cell migration, invasion, and adhesion (36). However, the precise mechanisms underlying PNI in gallbladder cancer are still not completely elucidated. In this study, we utilized laser-capture microdissection coupled with high-sensitivity mass spectrometry to investigate the changes in the perineural niche induced by PNI. OGA was identified as being aberrantly upregulated in neurons following tumor invasion. Using a noncontact coculture system, we showed that tumor-derived EVs deliver OGA to neurons. This EV-delivered OGA deglycosylated RIPK1, thereby promoting its phosphorylation and triggering complex IIb signaling, ultimately leading to neuronal necroptosis. Intriguingly, the necroptotic DAMP HMGB1 fed back on tumoral RAGE receptors to complete a tumor-driven neural invasion loop. Our findings clarify how tumor EVs induce neuronal programmed death and identify a targetable mechanism for new gallbladder cancer therapies.

EVs are nanosized vesicles released by cells that transport various biomolecules and regulate the behavior of recipient cells (37, 38). As key mediators of intercellular communication, EVs have emerged as promising candidates in liquid biopsies. Recent research has highlighted the role of EVs in facilitating communication between tumor cells and their surroundings (39–41). The high metabolic activity and signaling requirements of neurons necessitate dynamic post-translational modifications, with O-GlcNAc modifications, regulated by OGT and OGA, playing a central role in neuronal energy sensing and stress responses (42–44). Neurons maintain high levels of O-GlcNAc, which help inhibit abnormal phosphorylation and maintain cellular homeostasis (45). In Alzheimer's disease, reduced O-GlcNAc is associated with tau protein hyperphosphorylation (46). OGT expression is notably elevated in neurons, particularly in synapses and nuclei, where it contributes to synaptic plasticity and transcriptional regulation (47).

In this study, tumor cells were found to transfer OGA to neurons via EVs, inhibiting RIPK1 glycosylation and promoting its phosphorylation, which in turn triggers neuronal necroptosis. RIPK1 was activated via the complex IIb pathway upon exogenous OGA regulation. Another key finding of this study was the identification of Ser440 in RIPK1 as crucial for O-GlcNAcylation. Mutations at this site disrupted the glycosylation–phosphorylation balance, altering RIPK1's interaction with OGA and its downstream signaling. Nevertheless, several limitations remained. Future work should test the generality of this mechanism across additional cancer types and pursue rigorous biochemical validation of the OGA–RIPK1 interaction. Recombinant enzyme substrate binding assays should serve as the primary approach for confirming the direct interaction between OGA and RIPK1. An intriguing finding of this study was that the RIPK1 331A mutation enhanced its interaction with OGA, whereas the 440A mutation weakened it. This opposite behavior at distinct glycosylation sites calls for further structural investigation of the protein. Meanwhile, the antagonism between glycosylation and phosphorylation modifications warrants further investigation.

HMGB1-driven RAGE signaling in tumor cells fuels PNI, and the RAGE inhibitor FPS-ZM1 synergistically augments gemcitabine efficacy in preclinical models, underscoring clinical potential. Although HMGB1–RAGE has been implicated in multiple malignancies, its mechanistic role in neurotropic tumors such as cholangiocarcinoma and pancreatic cancer remains to be fully elucidated (48–52). This study established the HMGB1–RAGE loop as a driver of PNI. However, the intracellular signaling cascades triggered by this axis remain elusive, and the canonical nodes of RAGE activation merit comprehensive elucidation. In subsequent work, we will verify this pathway in at least two neurotropic tumor types and will focus particularly on the intracellular signaling alterations elicited by HMGB1–RAGE activation. Although FPS-ZM1 effectively disrupted the HMGB1–RAGE loop in models of PNI, we acknowledge several inherent limitations of this strategy. Systemic RAGE inhibition may compromise RAGE-dependent immune surveillance, and off-target liabilities could undermine therapeutic benefit. Future work should therefore prioritize antibody–drug conjugates or nanoparticle-encapsulated delivery to confine drug exposure to the tumor microenvironment and deploy biomarker-enriched trials that select patients with high HMGB1/RAGE expression to maximize the therapeutic index.

In conclusion, gallbladder cancer transfers OGA to neurons via EVs, inhibiting RIPK1 glycosylation and promoting its phosphorylation. This activates the complex IIb pathway, inducing neuronal necroptosis. Neuronal rupture releases HMGB1, which activates the RAGE receptor on gallbladder cancer cells, enhancing PNI and establishing a feedback loop.

Data Availability

scRNA-seq data analyzed in this study were based on our previous study and obtained from NODE at OEP001237. All original code has been deposited at Code Ocean (https://codeocean.com/capsule/6464349/tree/v2). Any additional information required to reanalyze the data reported in this article is available from the lead contact upon request.

Authors' Disclosures

No disclosures were reported.

Authors' Contributions

J. Zhao: Resources, data curation, software, formal analysis, validation, investigation, visualization, methodology, writing–original draft. **J. Zhu:** Conceptualization, resources, data curation, software, formal analysis, funding acquisition, validation, investigation, visualization, writing–original draft. **Z. Yang:** Conceptualization, formal analysis, funding acquisition, validation, visualization, methodology, writing–original draft. **Y. Zhai:** Conceptualization, validation, visualization, methodology. **C. Zhao:** Conceptualization, validation. **Z. Lu:** Data curation, supervision, validation, investigation, visualization. **D. Shen:** Data curation. **Q. Tang:** Data curation, investigation. **X. Song:** Data curation, funding acquisition, investigation. **L. Jiang:** Data curation, investigation. **W. Dai:** Data curation, investigation. **Y. Wang:** Data curation, validation, investigation. **Y. Zhu:** Data curation. **L. Shi:** Software. **R. Bao:** Funding acquisition, validation. **Z. Geng:** Conceptualization, resources, data curation, validation, methodology, project administration, writing–review and editing. **Z. Wang:** Conceptualization, supervision, methodology, project administration, writing–review and editing. **S. Liu:** Conceptualization, supervision, funding

acquisition, validation, methodology, project administration, writing–review and editing. **W. Gong:** Conceptualization, supervision, methodology, writing–review and editing.

Acknowledgments

This has been a long and arduous study, and we thank all the authors for their efforts. This work was supported by the Young Scientists Fund of the National Natural Science Foundation of China (no. 82303289 to S. Liu, 82203735 to D. Shen, 82403527 to X. Song), the Shanghai Sailing Program (23YF1426000 to S. Liu), the Interdisciplinary Program of Shanghai Jiao Tong University (YG2024QNA19 to Z. Yang), the Natural Science Foundation of Xizang Autonomous Region [XZ2023ZR-ZY40(Z) to R. Bao], and the Gusu Health Talent Program (no. GSWS2022026 to D. Shen).

Note

Supplementary data for this article are available at Cancer Research Online (http://cancerres.aacrjournals.org/).

Received May 27, 2025; revised September 23, 2025; accepted December 17, 2025; posted first December 29, 2025.

References

1. Roa JC, García P, Kapoor VK, Maithel SK, Javle M, Koshiol J. Gallbladder cancer. Nat Rev Dis Primers 2022;8:69.
2. Baiu I, Visser B. Gallbladder cancer. JAMA 2018;320:1294.
3. Zhang Y, Zuo C, Liu L, Hu Y, Yang B, Qiu S, et al. Single-cell RNA-sequencing atlas reveals an MDK-dependent immunosuppressive environment in ErbB pathway-mutated gallbladder cancer. J Hepatol 2021;75:1128–41.
4. Bray F, Laversanne M, Sung H, Ferlay J, Siegel RL, Soerjomataram I, et al. Global cancer statistics 2022: GLOBOCAN estimates of incidence and mortality worldwide for 36 cancers in 185 countries. CA Cancer J Clin 2024;74:229–63.
5. Zhao J, Shi L, Yang Y, Zhu J, Zhou Z, Dong P, et al. Wu-mei-wan promotes ferroptosis in gallbladder cancer through STAT3 negative regulation: an integrated HPLC, proteomics, network pharmacology, and experimental validation study. J Ethnopharmacol 2025;347:119671.
6. Margonis GA, Gani F, Buettner S, Amini N, Sasaki K, Andreatos N, et al. Rates and patterns of recurrence after curative intent resection for gallbladder cancer: a multi-institution analysis from the US extra-hepatic biliary malignancy consortium. HPB (Oxford) 2016;18:872–8.
7. Feo CF, Cossu ML, Ginesu GC, Ginesu GC, Fancellu A, Scanu AM, et al. Perineural infiltration as a prognostic factor in surgically treated gallbladder cancer A single center experience and literature review. Ann Ital Chir 2017;88:485–90.
8. Yamaguchi R, Nagino M, Oda K, Kamiya J, Uesaka K, Nimura Y. Perineural invasion has a negative impact on survival of patients with gallbladder carcinoma. Br J Surg 2002;89:1130–6.
9. Madhusudhan KS. Perineural invasion in gallbladder cancer. Radiographics 2021;41:E161–2.
10. Lv TR, Hu HJ, Liu F, Ma WJ, Jin YW, Li FY. The significance of peri-neural invasion in patients with gallbladder carcinoma after curative surgery: a 10 year experience in China. Updates Surg 2023;75:1123–33.
11. Lv TR, Wang JK, Li FY, Hu HJ. Prognostic factors for resected cases with gallbladder carcinoma: a systematic review and meta-analysis. Int J Surg 2024;110:4342–55.
12. Li J, Kang R, Tang D. Cellular and molecular mechanisms of perineural invasion of pancreatic ductal adenocarcinoma. Cancer Commun (Lond) 2021;41:642–60.
13. Di Chiaro P, Nacci L, Arco F, Brandini S, Polletti S, Palamidessi A, et al. Mapping functional to morphological variation reveals the basis of regional extracellular matrix subversion and nerve invasion in pancreatic cancer. Cancer Cell 2024;42:662–81.e10.
14. Jurcak NR, Rucki AA, Muth S, Thompson E, Sharma R, Ding D, et al. Axon guidance molecules promote perineural invasion and metastasis of orthotopic pancreatic tumors in mice. Gastroenterology 2019;157:838–50.e6.
15. Cheng K, Pan J, Liu Q, Ji Y, Liu L, Guo X, et al. Exosomal lncRNA XIST promotes perineural invasion of pancreatic cancer cells via miR-211-5p/GDNF. Oncogene 2024;43:1341–52.
16. Zheng S, Hu C, Lin Q, Li T, Li G, Tian Q, et al. Extracellular vesicle-packaged PIAT from cancer-associated fibroblasts drives neural remodeling by mediating m5C modification in pancreatic cancer mouse models. Sci Transl Med 2024;16:eadi0178.
17. Zhi X, Wu F, Qian J, Ochiai Y, Lian G, Malagola E, et al. Nociceptive neurons promote gastric tumour progression via a CGRP-RAMP1 axis. Nature 2025;640:802–10.
18. Tian Z, Ou G, Su M, Li R, Pan L, Lin X, et al. TIMP1 derived from pancreatic cancer cells stimulates schwann cells and promotes the occurrence of perineural invasion. Cancer Lett 2022;546:215863.
19. Yang MW, Tao LY, Jiang YS, Yang JY, Huo YM, Liu DJ, et al. Perineural invasion reprograms the immune microenvironment through cholinergic signaling in pancreatic ductal adenocarcinoma. Cancer Res 2020;80:1991–2003.
20. Wang H, Huo R, He K, Cheng L, Zhang S, Yu M, et al. Perineural invasion in colorectal cancer: mechanisms of action and clinical relevance. Cell Oncol (Dordr) 2024;47:1–17.
21. Schmitd LB, Perez-Pacheco C, Bellile EL, Wu W, Casper K, Mierzwa M, et al. Spatial and transcriptomic analysis of perineural invasion in oral cancer. Clin Cancer Res 2022;28:3557–72.
22. Shipley MM, Mangold CA, Szpara ML. Differentiation of the SH-SY5Y human neuroblastoma cell line. J Vis Exp 2016:53193.
23. Xu R, Greening DW, Zhu HJ, Takahashi N, Simpson RJ. Extracellular vesicle isolation and characterization: toward clinical application. J Clin Invest 2016;126:1152–62.
24. Richner M, Gonçalves NP, Jensen PH, Nyengaard JR, Vægter CB, Jan A. Recombinant adeno-associated virus mediated gene delivery in the extracranial nervous system of adult mice by direct nerve immersion. STAR Protoc 2022;3:101181.
25. Yan L, Zhang T, Wang K, Chen Z, Yang Y, Shan B, et al. SENP1 prevents steatohepatitis by suppressing RIPK1-driven apoptosis and inflammation. Nat Commun 2022;13:7153.
26. El-Mesery M, Shaker ME, Elgaml A. The SMAC mimetic BV6 induces cell death and sensitizes different cell lines to TNF-α and TRAIL-Induced apoptosis. Exp Biol Med (Maywood) 2016;241:2015–22.
27. Hannes S, Abhari BA, Fulda S. Smac mimetic triggers necroptosis in pancreatic carcinoma cells when caspase activation is blocked. Cancer Lett 2016;380:31–8.
28. Wang JH, Tseng CL, Lin FL, Chen J, Hsieh EH, Lama S, et al. Topical application of TAK1 inhibitor encapsulated by gelatin particle alleviates corneal neovascularization. Theranostics 2022;12:657–74.
29. Yang Y, Fang H, Xie Z, Ren F, Yan L, Zhang M, et al. Yersinia infection induces glucose depletion and AMPK-dependent inhibition of pyroptosis in mice. Nat Microbiol 2024;9:2144–59.
30. Zeng X, Chen Z, Zhu Y, Liu L, Zhang Z, Xiao Y, et al. O-GlcNAcylation regulation of RIPK1-dependent apoptosis dictates sensitivity to sunitinib in renal cell carcinoma. Drug Resist Updat 2024;77:101150.
31. Ma J, Wu C, Hart GW. Analytical and biochemical perspectives of protein O-GlcNAcylation. Chem Rev 2021;121:1513–81.
32. Coussement P, Bauwens D, Peters G, Maertens J, De Mey M. Mapping and refactoring pathway control through metabolic and protein engineering: the hexosamine biosynthesis pathway. Biotechnol Adv 2020;40:107512.
33. Yuan J, Ofengeim D. A guide to cell death pathways. Nat Rev Mol Cell Biol 2024;25:379–95.
34. Zhao J, Hou Y, Xie T, Zhu Y, Feng X, Zhang Y, et al. Genome-wide Mendelian randomization identifies putatively causal gut microbiota for multiple peptic ulcer diseases. Front Immunol 2023;14:1260780.
35. Zhang M, Huang Y, Pan J, Sang C, Lin Y, Dong L, et al. An inflammatory checkpoint generated by IL1RN splicing offers therapeutic opportunity for KRAS-mutant intrahepatic cholangiocarcinoma. Cancer Discov 2023;13:2248–69.
36. Baruch EN, Gleber-Netto FO, Nagarajan P, Rao X, Akhter S, Eichwald T, et al. Cancer-induced nerve injury promotes resistance to anti-PD-1 therapy. Nature 2025;646:462–73.
37. van Niel G, D'Angelo G, Raposo G. Shedding light on the cell biology of extracellular vesicles. Nat Rev Mol Cell Biol 2018;19:213–28.

38. Dixson AC, Dawson TR, Di Vizio D, Weaver AM. Context-specific regulation of extracellular vesicle biogenesis and cargo selection. Nat Rev Mol Cell Biol 2023;24:454–76.
39. Marar C, Starich B, Wirtz D. Extracellular vesicles in immunomodulation and tumor progression. Nat Immunol 2021;22:560–70.
40. Maacha S, Bhat AA, Jimenez L, Raza A, Haris M, Uddin S, et al. Extracellular vesicles-mediated intercellular communication: roles in the tumor microenvironment and anti-cancer drug resistance. Mol Cancer 2019;18:55.
41. Wu Y, Ma J, Yang X, Nan F, Zhang T, Ji S, et al. Neutrophil profiling illuminates anti-tumor antigen-presenting potency. Cell 2024;187:1422–39.e24.
42. Wang H, Vant JW, Zhang A, Sanchez RG, Wu Y, Micou ML, et al. Organization of a functional glycolytic metabolon on mitochondria for metabolic efficiency. Nat Metab 2024;6:1712–35.
43. Yu SB, Wang H, Sanchez RG, Carlson NM, Nguyen K, Zhang A, et al. Neuronal activity-driven O-GlcNAcylation promotes mitochondrial plasticity. Dev Cell 2024;59:2143–57.e9.
44. Huynh DT, Tsolova KN, Watson AJ, Khal SK, Green JR, Li D, et al. O-GlcNAcylation regulates neurofilament-light assembly and function and is perturbed by Charcot-Marie-Tooth disease mutations. Nat Commun 2023;14:6558.
45. Fan J, Guo F, Mo R, Chen LY, Mo JW, Lu CL, et al. O-GlcNAc transferase in astrocytes modulates depression-related stress susceptibility through glutamatergic synaptic transmission. J Clin Invest 2023;133:e160016.
46. Pinho TS, Verde DM, Correia SC, Cardoso SM, Moreira PI. O-GlcNAcylation and neuronal energy status: implications for alzheimer's disease. Ageing Res Rev 2018;46:32–41.
47. Park J, Kim DY, Hwang GS, Han IO. Repeated sleep deprivation decreases the flux into hexosamine biosynthetic pathway/O-GlcNAc cycling and aggravates alzheimer's disease neuropathology in adult zebrafish. J Neuroinflammation 2023;20:257.
48. Luo Y, Yoneda J, Ohmori H, Sasaki T, Shimbo K, Eto S, et al. Cancer usurps skeletal muscle as an energy repository. Cancer Res 2014;74:330–40.
49. Wang W, Chapman NM, Zhang B, Li M, Fan M, Laribee RN, et al. Upregulation of PD-L1 via HMGB1-activated IRF3 and NF-κB contributes to UV radiation-induced immune suppression. Cancer Res 2019;79:2909–22.
50. Mukherjee A, Vasquez KM. Targeting chromosomal architectural HMGB proteins could be the next frontier in cancer therapy. Cancer Res 2020;80:2075–82.
51. Nasser MW, Wani NA, Ahirwar DK, Powell CA, Ravi J, Elbaz M, et al. RAGE mediates S100A7-induced breast cancer growth and metastasis by modulating the tumor microenvironment. Cancer Res 2015;75:974–85.
52. Yeon M, Perego M, Elokely KM, Abou-Gharbia M, Childers WE, Milcarek AT, et al. Parkin induces ubiquitination and large extracellular vesicle release of HMGB1 to activate antitumor immunity. Cancer Res 2025;85:5033–48.